Tectonics®

RESEARCH ARTICLE
10.1029/2025TC009286

Key Points:

- We re-analyzed the 1906 Manas and 1944 Xinyuan earthquake magnitudes and hypocenters using archival seismogram and global seismic records
- We combined previous studies with our seismological analysis of historical earthquakes to examine the Borohoro Shan (BRS) seismotectonics
- Most common surface deformations from significant historical earthquakes near BRS are landslides instead of fault scarps

Supporting Information:

Supporting Information may be found in the online version of this article.

Correspondence to:

C.-H. Tsai,
ts933470@reading.ac.uk

Citation:

Tsai, C.-H., Kulikova, G., Krüger, F., & Walker, R. T. (2026). Source parameters of the 1906 Manas (Mw 7.7), 1944 Xinyuan (Mw 7.2) and 1812 Nilke earthquakes and seismotectonics of the Borohoro Shan, western China. *Tectonics*, *45*, e2025TC009286. https://doi.org/10.1029/2025TC009286

Received 3 DEC 2025
Accepted 23 MAY 2026

Author Contributions:

Conceptualization: C.-H. Tsai, G. Kulikova, F. Krüger, R. T. Walker
Data curation: G. Kulikova, F. Krüger
Formal analysis: G. Kulikova
Funding acquisition: F. Krüger, R. T. Walker
Investigation: C.-H. Tsai, G. Kulikova
Methodology: C.-H. Tsai, G. Kulikova, F. Krüger, R. T. Walker
Project administration: F. Krüger, R. T. Walker
Resources: F. Krüger, R. T. Walker
Software: G. Kulikova
Supervision: F. Krüger, R. T. Walker
Validation: G. Kulikova, F. Krüger, R. T. Walker

© 2026. The Author(s).
This is an open access article under the terms of the Creative Commons Attribution License, which permits use, distribution and reproduction in any medium, provided the original work is properly cited.

Source Parameters of the 1906 Manas (Mw 7.7), 1944 Xinyuan (Mw 7.2) and 1812 Nilke Earthquakes and Seismotectonics of the Borohoro Shan, Western China

C.-H. Tsai[1,2], G. Kulikova[3], F. Krüger[4], and R. T. Walker[1]

[1]COMET, Department of Earth Sciences, University of Oxford, Oxford, UK, [2]National Centre for Atmospheric Science, University of Reading, Reading, UK, [3]UP Transfer GmbH at the University of Potsdam, Potsdam, Germany, [4]Institute of Geosciences, University of Potsdam, Potsdam, Germany

Abstract The 1906 Manas Earthquake is the largest earthquake recorded in the Borohoro Shan (BRS) since 1900. The reported magnitude ranges from 7.2 to 8.3, but uncertainties remain regarding its size, mechanism, and responsible fault. Similar confusion exists for the 1812 Nilke and 1944 Xinyuan Earthquakes, the only other Mw > 7 earthquakes in the NE Tien Shan in China. To address this, we compiled and analyzed prior published data and conducted remote sensing mapping for these historical events. Through re-analysis of the 1906 Manas and 1944 Xinyuan Earthquakes using archival seismogram and global seismic records, we relocated the hypocenter of the 1906 event and determined the magnitude to be Mw 7.7 ± 0.2. Based on the revised results and seismic profiles, we infer the earthquake likely originated from a steeply south-dipping reverse fault beneath the BRS, with northward propagation to the surface along a shallow decollement. Our analysis of the 1944 earthquake suggests it comprised a Mw 6.5 ± 0.3 foreshock and a Mw 7.2 ± 0.2 main shock after 9 min, both exhibiting dominant strike-slip motion. The 1812 earthquake, recorded in the official historical archives mentioning severe shaking and damages, is likely to have an overestimated magnitude and to result from both reverse and right-lateral slip along the Kashihe Fault. These earthquakes emphasize the significance of seismic-induced landslides and the presence of right-lateral and reverse faulting in the seismotectonics of the BRS region.

1. Introduction

The 1906 Manas Earthquake occurred at the northern tip of the Chinese Tien Shan, along the northern margin of the BRS and the southern margin of the Dzhungarian (Junggar) basin (Figure 1) (Avouac et al., 1993; Molnar & Deng, 1984; Institute of Geophysics, SSB and Institute of Chinese Historical Geography, 1990; Zhang et al., 1994). It is one of the largest (Ms ≈ 8) reverse faulting earthquakes known on the continents, potentially involving the rupture of multiple segments, and with inferred complexities of rupture with depth (Avouac et al., 1993; Burchfiel et al., 1999; Deng et al., 1996, 2000; Stockmeyer et al., 2014; Wang et al., 2004). The 1906 earthquake is well recorded in historical documents and has a wide coverage of recorded intensities (Institute of Geophysics, SSB & Institute of Chinese Historical Geography, 1990). However, the surface ruptures inferred to be caused by this event are scarce and widely distributed (Avouac et al., 1993). Moreover, estimates of its epicenter and magnitude vary widely (Figure 2 and Table 1). Reported magnitudes range from 7.2 to 8.3, depending on the magnitude scale and input data used. Other large-magnitude earthquakes have occurred within the BRS (Figures 1b and 2). The 1944 Xinyuan Earthquake (Mw 7.1 from USGS) is thought to have occurred within the southwestern part of the range, but with reported epicenter locations differing by up to ∼100 km (Yang, 1992; Shen et al., 2003; Chinese Earthquake Network Center (CENC)), meaning that the causative fault, or faults, are unknown (Figure 2). The 1812 Nilke Earthquake is suggested to have even higher intensity than the 1906 Manas Earthquake but with little information about its magnitude and earthquake mechanism (Yang et al., 1985; Yin et al., 2009).

These three events highlight the non-negligible seismic hazards around the BRS but all have unclarified magnitudes, epicenters, or causative faults that are critical to understanding the seismotectonics of the BRS and the occurrence of large intraplate earthquakes in general, as well as the regional active tectonics of central Asia. Furthermore, the regions bordering the BRS have seen dramatic population increase and urban growth over past decades. Urumqi, with a population of over 4 million, lies to the northeast, while smaller but rapidly growing cities, such as Shihezi, lie to the north of the BRS. In the south, the Ili region has a population of over 2.7 million

Visualization: C.-H. Tsai, G. Kulikova
Writing – original draft: C.-H. Tsai, G. Kulikova
Writing – review & editing: C.-H. Tsai, G. Kulikova, F. Krüger, R. T. Walker

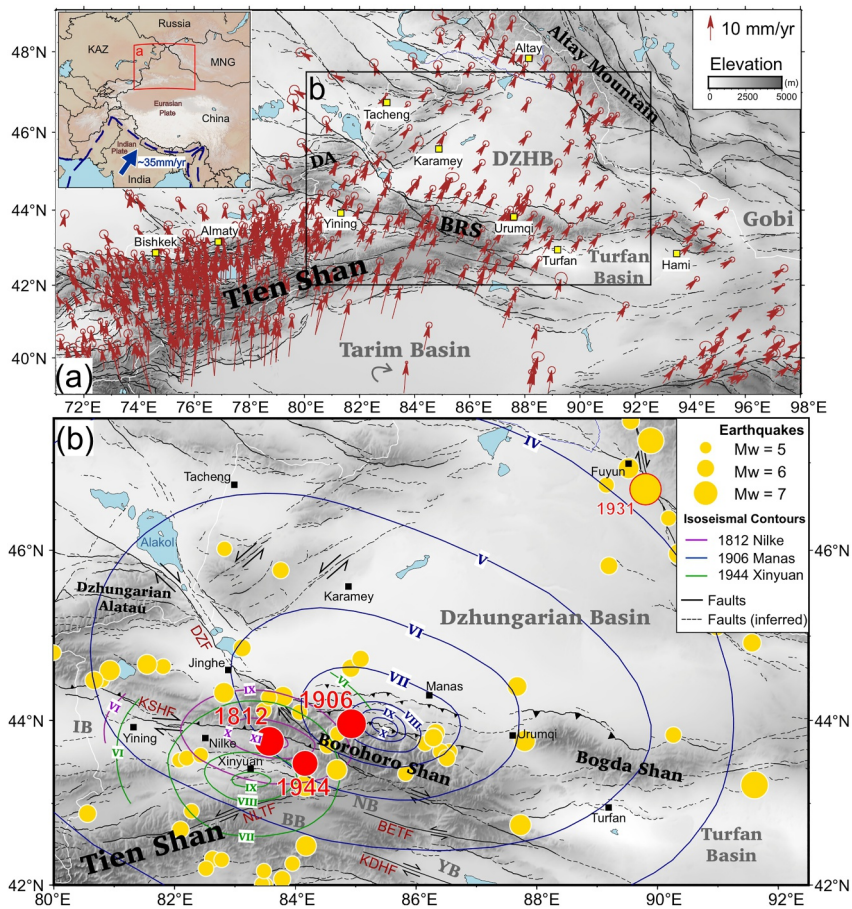

Figure 1. (a) Overview of the Tien Shan with its surrounding mountains and basins. GPS velocity vectors (brown) are from Zubovich et al. (2010) and Wang and Shen (2020). Cities and towns are labeled with yellow squares. International borders are in white. BRS: Borohoro Shan; DA: Dzhungarian (Junggar) Alatau; DZHB: Dzhungarian (Junggar) Basin; KAZ: Kazakhstan; MNG: Mongolia. The inset map shows that the Indian plate is moving NNE at ~35 mm/yr relative to the Eurasian plate (Abdrakhmatov et al., 1996; England & Molnar, 1997). The blue dashed line indicates the plate boundary. (b) Overview of seismicity around the Dzhungarian Basin. Yellow circles are earthquakes with magnitudes above 5.5 between 1904 and 2017 in the ISC-GEM catalog (ISC, 2021). The 1812 Nilke, 1906 Manas and 1944 Xinyuan events are highlighted as red circles with the epicenter locations explained in context within the text. The isoseismal maps of the 1812, 1906 and 1944 earthquakes are displayed in purple, blue and green lines with the intensity labeled in New Chinese Intensity Scale (Institute of Geophysics, SSB & Institute of Chinese Historical Geography, 1990; Yang, 1992; Yin et al., 2009). The 1931 Mw 7.6 Fuyun Earthquake (Klinger et al., 2011) is highlighted by a red frame. Cities and towns are labeled in black squares. Fault locations are based on the mapping in Avouac et al. (1993) and the online database from Zelenin et al. (2021). The names of the main strike-slip faults are noted in brown: DZF: Dzhungarian Fault; KSHF: Kashihe Fault; NLTF: Nalati Fault; BETF: Baoertu Fault; KDHF: Kaiduhe Fault. IB: Ili Basin; NB: Nalati Basin; BB: Bayanbuluk Basin; YB: Yangqi Basin.

and contains rapidly developing cities such as Tekesi and Yining, and lies directly adjacent to the Borohoro range and its active fault systems. This brings a necessity for investigating the potential sources of future earthquakes through an understanding of examples from recent history, and through evidence preserved in the late Quaternary geology.

In this study, we better constrain the rupture extent, responsible faults, and fault mechanisms for the three historical events by compiling new evidence and existing observations. We analyze the 1906 and 1944 earthquake source parameters and integrate them with geological observations from the published literature. We located and compiled the previously reported surface ruptures caused by the 1812, 1906, and 1944 earthquakes and summarized them with our own examination from open-access high-resolution modern satellite imagery. We then relocated the hypocenters for the 1906 and 1944 earthquakes and re-estimated their magnitudes by analyzing archival analogue seismograms and global seismic records. This seismological approach has been successfully

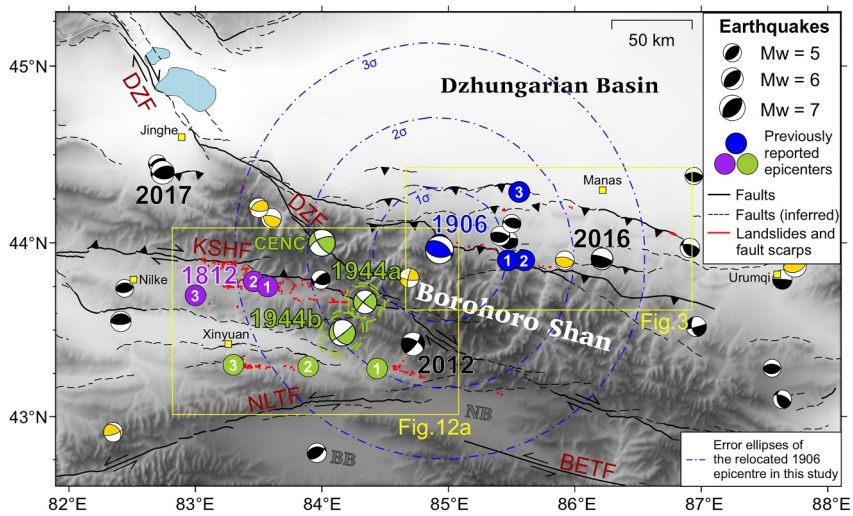

Figure 2. Tectonic overview of the Borohoro Shan and the 1812, 1906 and 1944 earthquakes. Focal mechanisms of historical earthquakes are shown in yellow for those analyzed by Sloan et al. (2011) and in black for those from 1976 to June of 2021 with Mw > 5 from the Global Centroid-Moment-Tensor (GCMT) data (Dziewonski et al., 1981; Ekström et al., 2012). The previously reported epicenters for the 1812 event (purple circles) are numbered "1" by Yin et al. (2009), "2" by Yang et al. (1985) and "3" by China Earthquake Administration (1971). The previously reported epicenters for the 1906 event (blue circles) are numbered "1" by Xie and Cai (1986), "2" by the Institute of Geophysics, SSB & Institute of Chinese Historical Geography (1990) and "3" by Storchak et al. (2013). The focal mechanism for the 1906 event (in blue) is re-estimated by this study with the relocated epicenter and its error ellipses in 3 sigmas (blue dotted-dash lines). The previously reported epicenters for the 1944 event (green circles) are numbered "1" and "2" by the USGS catalog for the 1944a and 1944b events respectively, and "3" by Yang (1992). The 1944 epicenter and fault plane solutions from China Earthquake Networks Center (CENC) and this study, with error ellipses in 3 sigmas (green dotted-dash lines), are also labeled in green. Cities and towns are labeled in yellow squares. Fault locations are from Avouac et al. (1993), Ren et al. (2021) and Zelenin et al. (2021). Possibly earthquake-induced landslides and fault scarps mapped by the previous work and this study are labeled in red (Avouac et al., 1993; Feng, 1990; Yang, 1992; Yang et al., 1985; Yin et al., 2009; Zhang, Deng, Xu, Peng, et al., 1994, Zhang, Deng, Xu, Wu, et al., 1994). The 2012 Mw 6.3 Xinyuan, the 2017 Mw 6.3 Jinghe, and the 2016 Mw 6.0 Hutubi earthquakes are annotated in black. DZF: Dzhungarian Fault; KSHF: Kashihe Fault; NLTF: Nalati Fault; BETF: Baoertu Fault; NB: Nalati Basin; BB: Bayanbuluk Basin.

applied to other large intra-continental historical earthquakes in Asia (Kulikova & Krüger, 2015; Ou et al., 2020). Finally, we integrated the geological observations, isoseismal maps and sub-surface seismic reflection profiles with our seismological analysis results to propose the likely responsible faults and the kinematics for these three historical events and to highlight the seismotectonics of the BRS. This improved understanding of the source parameters and causative faults for historical earthquakes also helps provide a foundation for improved seismic hazard assessments relevant to the cities and infrastructure of the region.

2. Tectonic Settings and Earthquakes of the Borohoro Shan

The Tien Shan is a ~2,500-km-long E-W trending mountain range that straddles western China, SE Kazakhstan and Kyrgyzstan (Figure 1a). It has a long geological history, with initial deformation in the late Paleozoic, and with Cenozoic reactivation related to the India-Eurasian collision (Abdrakhmatov et al., 2001; De Grave et al., 2007; Molnar & Tapponnier, 1975; Windley et al., 1990, 2007). The BRS is a sub-range connecting the NW and the NE Tien Shan, which also separates the Dzhungarian (Junggar) Basin in the north from the Tarim basin in the south (Figure 1). A prominent fold and thrust belt along the northern margin of the BRS has deformed the thick Mesozoic and Cenozoic sedimentary strata of the Dzhungarian Basin (Figure 2) (Avouac et al., 1993; Burchfiel et al., 1999; Charreau et al., 2008; Daëron et al., 2007; Deng et al., 2000; Lu et al., 2018; Stockmeyer et al., 2017). This fold and thrust belt consists of three main subparallel anticlines formed in the Cenozoic with active reverse faults in listric geometries at their fronts (Lu et al., 2018; Stockmeyer et al., 2014; Su et al., 2018; Wang et al., 2004). From south to north, these are the Qigu, Tugulu-Manas-Huoerguos and Anjihai-Dushanzi anticlines and their corresponding faults (Figure 3a). The Holocene shortening rate is ~2.2–3.3 mm/yr at the Tugulu-Manas-Houergous Fault and ~1.3–2.0 mm/yr at the Anjihai-Dushanzi Fault (Fu et al., 2017; Su et al., 2018).

Tectonics

10.1029/2025TC009286

Table 1
Reported Magnitudes, Depths and Surface Rupture Length of the 1906 Manas Earthquake

Magnitudes	Reference	Method
Ms 7.9	Gutenberg and Richter (1954) and Abe (1981)	Surface wave amplitudes measured at 20s period
Ms 8.3	Richter (1958)	Surface wave amplitudes
m_B 7.5	Abe (1981)	Body wave amplitude measured on an instrument at periods of ∼ 4–12s.
M 8	Bai and Fang, (1981)	Unspecified
Ms 8	Gu (1983)	Referred to Gutenberg and Richter (1954) but with corrections based on Chinese seismological data
Ms 7.2	Abe and Noguchi (1983)	Surface wave amplitudes corrected by a factor of the effective gain of the instruments
Ms 8.3	Molnar and Deng (1984)	Rupture area based on the observations in Bai and Fang, (1981)
Ms 7.3	Abe (1988)	Revised from Abe and Noguchi (1983)
Ms 8 ± 0.2	Avouac et al. (1993)	Rupture area from field observations and associated assumptions
Ms 7.7	Institute of Geophysics, SSB & Institute of Chinese Historical Geography, (1990); Zhang, Deng, Xu, Peng, et al. (1994); Deng et al. (1996); Yang et al. (1998); Yang et al. (2002); Zhou et al. (2003); Wang et al. (2004); Lu et al. (2018)	Either unspecified or refer to the field survey conducted by the Seismological Bureau of Xinjiang Uygur Autonomous Region in 1973
Mw 7.8 ± 0.2	Storchak et al. (2013)	Method see Storchak et al. (2013)
Mw 7.95	ISC-GEM (2021)	Original amplitude-period measurements (Bondár et al., 2015)
m_B 7.4 ± 0.3 M_S 7.9 ± 0.2 Mw 7.7 ± 0.2	This study	Methods elaborated in this study based on Kulikova (2016)

Depth	Reference	Method
12 km	Gu (1983)	Unspecified but should be related to the formula in Gutenberg and& Richter (1942) and Liu (1961)
24 km	Xie and Cai (1986)	Referring to the Chinese earthquake catalog in 1977
15–40 km	Avouac et al. (1993)	Compilation of the depths from historical seismicities in the northern Tien Shan
∼15 km	Yang et al. (2002)	Tomography profiles and the depths from historical seismicities
20 km	Wang et al. (2004)	The median focal depth from 110 well-located earthquakes in the northern Tien Shan since 1980.
18 km	This study	Methods elaborated in this study based on Kulikova (2016)

Surface Rupture Length	Reference	Method
65 km	Bai and Fang, (1981)	Observation of ruptures from the Shiaonangou River to the east of the Manas River
40 km	Molnar and Deng (1984)	The most concentrated area of ruptures mentioned in Bai and Fang, (1981)
150 km	Avouac et al. (1993)	The length from South Anjihai Anticline to Tugulu Anticline
130 km	This study	Distance between the east of the Anjihai River and the west of the Hutubi River
110–120 km	This study	Source duration based on the P-wave recording

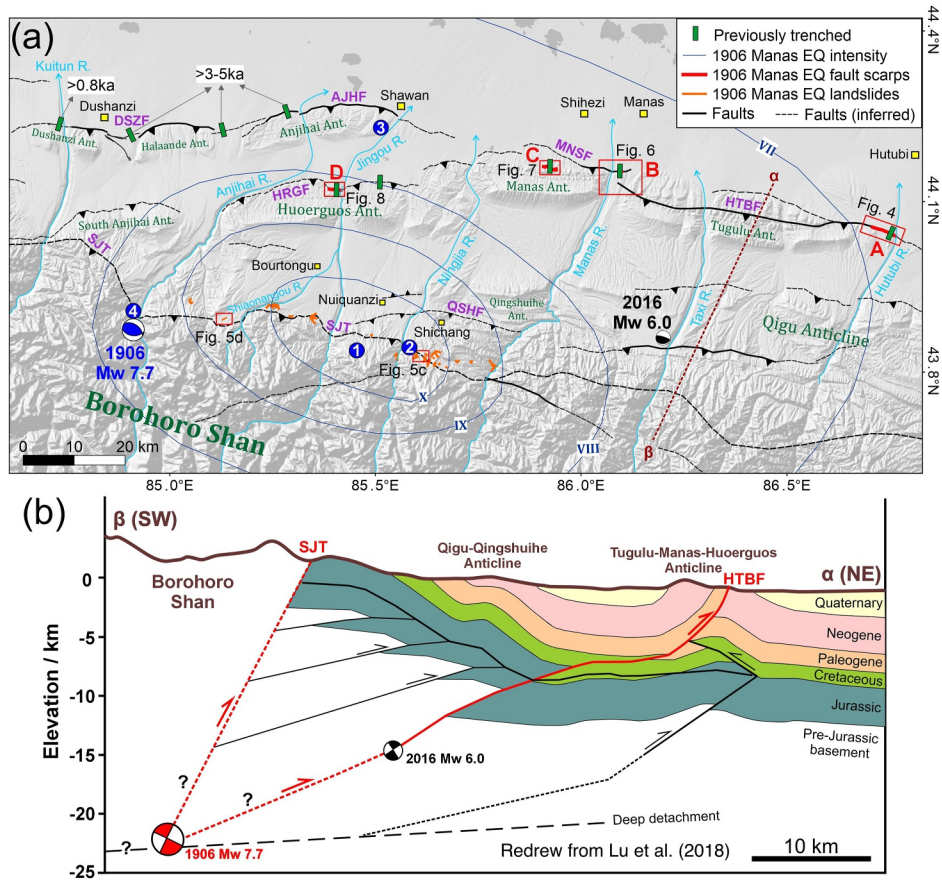

Figure 3. (a) Topographic map showing the fold and thrust belt at the northern range front of the Borohoro Shan from the shaded ESRI world relief imagery. A (Hutubi River west), B (Manas River east), C (Aweitan) and D (Jinguo River west) are the four regions where the 1906 possible fault scarps (red lines) are found. The detached scarps and landslides likely caused by the 1906 event are labeled in orange. Previous trenching sites (green rectangles) (Deng et al., 1996; Su et al., 2018) are shown with the ages of their most recent earthquakes summarized and noted. Names of the anticlines (Ant.) and mountain ranges are annotated in green text. Isoseismal map (blue lines) of the 1906 earthquake is displayed with the intensity in New Chinese Intensity Scale (Institute of Geophysics, SSB & Institute of Chinese Historical Geography, 1990). Previously-located epicenters are in blue circles with the number "4" from the ISC-GEM catalog (ISC, 2021) and the others described in the caption of Figure 2. The focal mechanism of the 1906 event (in blue) from this study and the 2016 Mw 6.0 Hutubi Earthquake from Lu et al. (2018) are marked. Cities and towns are labeled in yellow and noted by black text. Major rivers are labeled in light blue with arrows. The brown dashed line marks the path of the seismic-reflection profile (α-β) shown in (b). Names of the reverse faults are annotated by purple text. SJT: Southern Junggar Thrust; QSHF: Qingshuihe Fault; HRGF: Huoergous Fault; DSZF: Dushanzi Fault; AJHF: Anjihai Fault; MNSF: Manas Fault; HTBF: Hutubi Fault (HTF). Fault locations are compiled from Avouac et al. (1993), Zelenin et al. (2021) and our own mapping results. (b) Seismotectonic model modified from Lu et al. (2018), based on a ~15 km-deep seismic-reflection profile of the Borohoro range front, for the 1906 Manas Earthquake and the 2016 Hutubi Earthquake. Red lines represent the likely ruptured faults during the 1906 Manas Earthquake. (Dashed red lines are the inferred faults.) Brown lines represent the topography. HTBF: HTF.

Besides those reverse structures accommodating the crustal deformation via shortening, large strike-slip faults accommodate the counterclockwise rotation of the NW Tien Shan tectonic blocks and left-lateral shear in the eastern Tien Shan (Figure 2) (Cunningham, 2007; Wu et al., 2021). The right-lateral strike-slip Dzhungarian Fault (also called the Bolokenu-Aqikekuduk Fault, or Bo-A, Fault, e.g. Shen et al., 2003; Z. Hu, Li, et al., 2021) enters the BRS from the northwest and probably merges with the oblique right-lateral and reverse Kashihe Fault (Kashi River (KSR) Fault) that is ~WNW-ESE trending and located at the southwestern margin of the BRS (Figure 2) (Z. Hu, Li, et al., 2021; Wu et al., 2020). The right-lateral slip rate of the Kashihe Fault is ~2.4 mm/yr with a shortening rate of ~0.6 mm/yr (Wu et al., 2020), and the DZF has a right-lateral slip rate of 2.1–4.7 mm/yr in the south with an uplift rate of 0.6 ± 0.2 mm/yr in the north (Campbell et al., 2013; Z. Hu, Li, et al., 2021, this study) (Figure 2). Another WNW-ESE trending right-lateral strike-slip fault is the Kaiduhe Fault which is located in the

southeastern BRS with a dextral slip rate of 1.2–1.6 mm/yr (Huang, 2015) (Figure 1b). The WSW-ENE trending left-lateral and reverse Nalati Fault extend s from the southern margin of the BRS to the Kyrgyz Tien Shan with a strike-slip rate of 1.4–1.8 mm/yr and a shortening rate of 1.4 ± 0.7 mm/yr (Charreau et al., 2017). Another left-lateral strike-slip fault is the ∼E-W trending Baoertu Fault that is located in the southeastern BRS with a left-lateral slip rate of ∼0.65 ± 0.16 mm/yr and shortening rate of ∼0.07 ± 0.01 mm/yr (Ren et al., 2021) (Figure 1b). These left-lateral strike-slip faults are considered to be parts of the Gobi-Tien Shan fault system that is accommodating the left-lateral shearing across the NE Tien Shan and Gobi region (Cunningham, 2007) (Figure 1a).

Almost 80 earthquakes with magnitudes ≥5.0 (Wang et al., 2004) and at least 19 events with magnitudes ≥6.0 in any magnitude scale (Z. Hu, Li, et al., 2021; ISC, 2022b) have occurred around the BRS in the past three centuries. Most of the historical events in the northern BRS fold and thrust belt are reverse or thrust events such as the latest 2017 Mw 6.3 Jinghe and the 2016 Mw 6.0 Hutubi Earthquakes (Figure 2) (Dziewonski et al., 1981; Ekström et al., 2012; ISC, 2022b). The 2017 Jinghe Earthquake occurred on the lower ramp of the south-dipping Jinghenan Fault with the maximum slip at a depth of ∼14 km but without surface rupture (Figure 2) (Gong et al., 2019; Z. Hu, Yang, et al., 2021). The 2016 Hutubi Earthquake occurred under the Qigu-Qingshuihe Anticline at a depth of ∼16 km along the Tugulu-Manas-Huoerguos Fault or on a north dipping back-thrust of it (Figures 2 and 3) (Lu et al., 2018; Wang et al., 2019). This 2016 earthquake did not cause surface rupture, but it did lead to a destruction of infrastructures and serious economic losses (Wang et al., 2019). Most of the past events in the southern BRS have prominent strike-slip mechanisms compared to the northern ones such as the recent 2012 Mw 6.3 Xinyuan Earthquake (Dziewonski et al., 1981; Ekström et al., 2012). This 2012 earthquake is a right-lateral strike-slip event and possibly ruptured the Kashihe Fault, with a hypocentral depth of ∼28 km (Figure 2) (Wang et al., 2015).

The three largest earthquakes recorded around the BRS, with magnitudes >7.0, are the 1906 Manas Earthquake in the north, and the 1944 Xinyuan and 1812 Nilke Earthquakes in the south, which all have the highest intensity above IX in New Chinese Intensity Scale (Figure 1b) (Institute of Geophysics, SSB & Institute of Chinese Historical Geography, 1990; Yang, 1992). The 1906 and the 1812 events have similar degrees of damage and have been initially estimated to have magnitudes above or approaching Ms 8 (Table 1) (Bai & Fang, 1981; Richter, 1958; Yang et al., 1985). The 1944 event is a smaller event with a better-estimated magnitude of Mw 7.1–7.3 and has been reported to be a double-event earthquake (https://www.usgs.gov/natural-hazards/earthquakes), but it has widely distributed estimates of epicenters compared to the other two (Figure 2).

3. The 1906 Manas Earthquake

3.1. Background and Macroseismic Data

The Manas Earthquake occurred at 18:21:12 UTC on 22nd December 1906. It caused the collapse of more than 2100 houses and at least 305 fatalities (Institute of Geophysics, SSB & Institute of Chinese Historical Geography,1990; Zhang, Deng, Xu, Peng, et al., 1994). The estimated magnitudes for this earthquake range from M 7.2–8.3 in various scales (Table 1). (Abe, 1988; Abe & Noguchi, 1983; Avouac et al., 1993; Bai & Fang, 1981; Burchfiel et al., 1999; Gu, 1983; Gutenberg & Richter, 1954; Institute of Geophysics, SSB & Institute of Chinese Historical Geography, 1990; ISC, 2021; Molnar & Deng, 1984; Richter, 1958; Stockmeyer et al., 2014; Xie & Cai, 1986). It is the latest and the most destructive historical event with a magnitude >7 at the northern range front of the BRS and further aftershocks were recorded in the following six years until 1912 (Institute of Geophysics, SSB & Institute of Chinese Historical Geography, 1990). The first detailed investigation of the surface ruptures and isoseismal map of this earthquake was conducted from 1972–1980 by the Seismological Bureau of Xinjiang Uygur Autonomous Region (Bai & Fang, 1981; Institute of Geophysics, SSB & Institute of Chinese Historical Geography, 1990). According to those studies, ground shaking reached X in the New Chinese Intensity Scale for the area near Nuiquanzi, reached VI at the capital city Urumqi and reached V or IV for regions near Turfan, Yining, Tacheng and Lake Alakol (Figure 1b). The most damaged area is in the southwest of the current Manas County including Shichang, Nuiquanzi and Bo'ertonggu where all the mud-built houses and 90% of the wooden houses were destroyed (Institute of Geophysics, SSB & Institute of Chinese Historical Geography, 1990) (Figure 3). The epicenter inferred from the isoseismal map is near 43.9°N, 85.6°E (Institute of Geophysics, SSB & Institute of Chinese Historical Geography, 1990) or 43.9°N, 85.47°E (Xie & Cai, 1986). On the other hand, the ISC has provided epicentral locations at 44.2°N, 85.56°E (Storchak et al., 2013) and 43.99°N, 84.93°E (ISC, 2021) (Figure 3).

Most of the inferred surface ruptures from the 1906 event are landslides and fractures triggered by shaking and gravity instead of the direct movements of the fault (Bai & Fang, 1981; J. Hu & Bai, 1988; Seismological Bureau of Xinjiang, 1985; Zhang, Deng, Xu, Peng, et al., 1994). Several fault scarps possibly ruptured by the 1906 Manas Earthquake are all sited 30–90 km northeast of the inferred epicenters (Figure 3a) (Avouac et al., 1993; Deng et al., 1996; Pang et al., 2021; Zhang, Deng, Xu, Peng, et al., 1994, Zhang, Deng, Xu, Wu, et al., 1994), albeit some authors disagree with those distant scarps being products of the 1906 event (Burchfiel et al., 1999), highlighting the continued challenges in identifying the responsible fault. Based on the isoseismal map and the epicenters inferred from it, some studies have attributed the 1906 earthquake to the Qingshuihe Fault or the Southern Junggar Thrust (SJT) (also called the Junggar Frontal Thrust or the Junggar Southern Marginal Fault), which is a ~E-W trending reverse fault dipping to the south (Figure 3a) (Avouac et al., 1993; Bai & Fang, 1981; J. Hu & Bai, 1988; Wang et al., 2004). Others attribute the earthquake to a blind fault underneath the range front of the BRS (Deng et al., 1996; Zhang, Deng, Xu, Peng, et al., 1994, Zhang, Deng, Xu, Wu, et al., 1994), though this does not rule out rupture at depth on the SJT (Yang et al., 1998). A number of studies have further revealed the complicated subsurface structures of this fold and thrust belt with two levels of decollements and several structural wedges with listric geometries and back thrusts, which certainly increases the number of candidates for the responsible fault of the 1906 Manas Earthquake (Li et al., 2011; Lu et al., 2018; Stockmeyer et al., 2014; Wang et al., 2004; Yang et al., 2002).

3.2. Surface Ruptures

According to the previous literature (Avouac et al., 1993; Bai & Fang, 1981; Deng et al., 1994; Deng et al., 1996; Seismological Bureau of Xinjiang, 1985; Zhang, Deng, Xu, Peng, et al., 1994, Zhang, Deng, Xu, Wu, et al., 1994), the possible 1906 surface ruptures expressed as fault scarps or flexural scarps have only been found in four places and the landslides caused by this earthquake are mostly found along the northern hills of the BRS near Shichang (Figure 3a). We assessed these sites from east to west and mapped ground deformation features that can still be recognized in the imagery. Fault scarps were identified as escarpments cutting across topography with visible vertical or lateral offset; landslides were identified by the presence of a crown-shaped main scarp, deposits, and toe.

3.2.1. Western Terraces of the Hutubi River

The northward-flowing Hutubi River is located at the eastern end of the E-W trending Hutubi Fault (HTF) that penetrates the Tugulu Anticline (Figure 3a). From the eastern part of the Tugulu Anticline to the western terraces of the Hutubi River, prominent fault scarps up to 8 km long can be recognized but no fault scarps are found on the eastern side of the river (Zhang, Deng, Xu, Peng, et al., 1994) (Figure 4). From a road cut on the eastern flank of Tugulu Anticline, Stockmeyer et al. (2014) observed at least two south-dipping fault splays underneath the fault scarp and suggested them to be the splays of the SJT from the interpretation of seismic-reflection profiles. In this study, we mapped the Hutubi River terraces and the HTF scarps based on the 30-m DEM from Copernicus imagery (Opentopography.org) and optical satellite imagery from Yandex Maps, Bing Maps and Google Earth (European Space Agency Sinergise, 2021) (Figure 4d). The terraces from high to low are labeled from T6 to T1 in this study with their approximate elevations as 890 m (T6), 820 m (T5), 816 m (T4), 813 m (T3), 796 m (T2), 776 m (T1) and 766 m (T0, riverbed) (Figure 4). Terrace T3 is the largest hanging-wall terrace surface cut by the fault with braided rivers still developing on it and T3′ is defined as the corresponding terrace surfaces on the footwall of the western bank that are flat and widely spread (Figure 4). We recognized from the 2019 Google Earth imagery that the hanging wall of T3 has been modified with concentric agricultural facilities so that the original topography is no longer preserved (Figures 4a and 4b). However, Avouac et al. (1993), Zhang, Deng, Xu, Peng et al. (1994) and Deng et al. (1996) presented in situ measurements for these fault scarps and some trench data in the 1990s before the artificial modification.

The average height of fault scarps between T3 and T3′ is 8.5 ± 0.2 m (Avouac et al., 1993) with a hinge graben preserved on the upper parts of some scarps. The scarp is typically composite, with the lowest scarp heights of 1.1 m (Avouac et al., 1993) or 0.30–0.58 m (Deng et al., 1994, 1996; Zhang, Deng, Xu, Peng, et al., 1994), inferred to represent the most recent surface rupture (Figures 5a and 5b). The fault scarps between T4 and T3′ are all composite scarps, suggestive of accumulated vertical offset, with an average height of 11.1 ± 0.6 m (Avouac et al., 1993). Deng et al. (1996) excavated a large trench (HUTc-1) consisting of nine stepped subtrenches on terrace T3 near 86.794°E, 44.045°N and they found three south-dipping reverse faults (F1, F2 and F3) and one

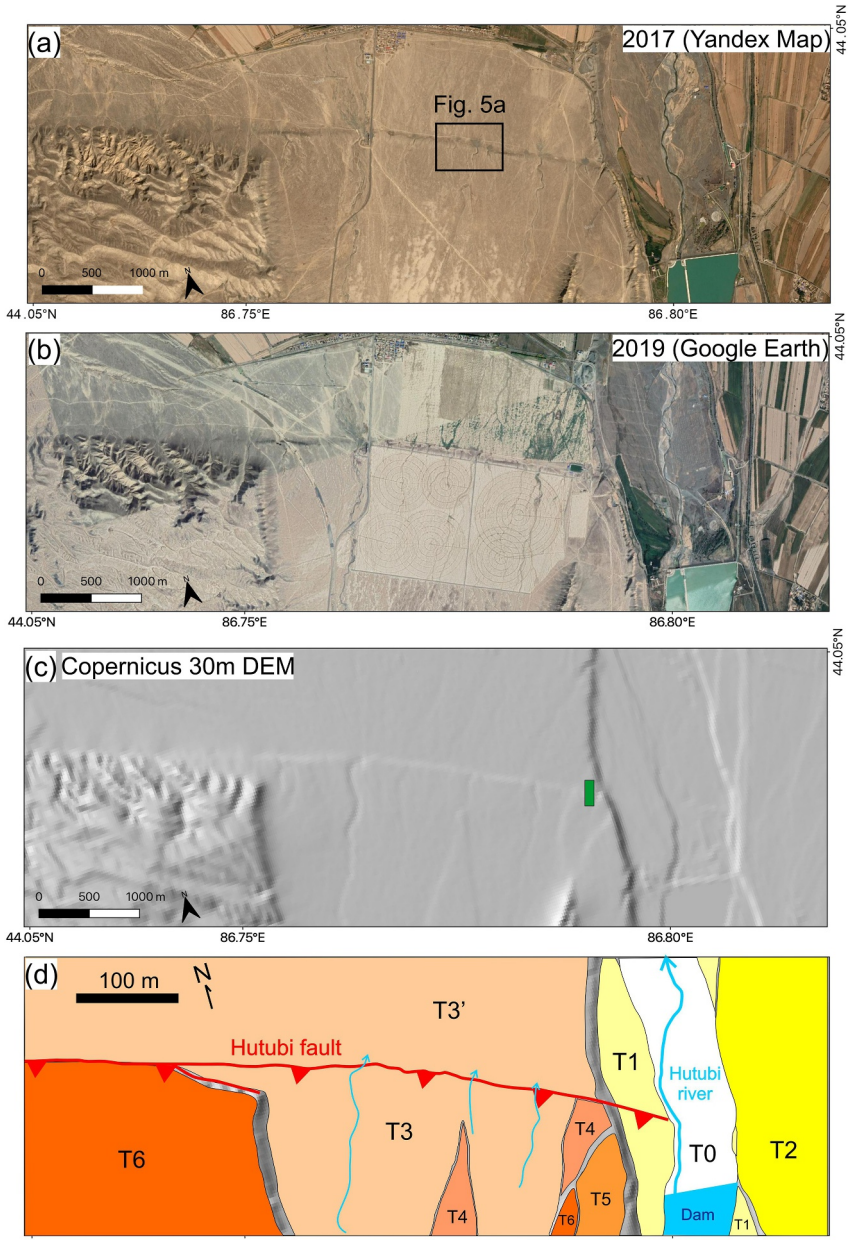

Figure 4. Fault scarps along the Hutubi Fault on the western bank of the Hutubi River (Region A in Figure 3). (a) and (b) Optical satellite imagery from Yandex and Google Earth Map (0.4 and 0.2 m resolution, respectively), with acquisition years noted. Artificial irrigation and farming systems can be seen from the 2019 imagery which has modified the original landscape. (c) Shaded topographic relief from the 30-m Copernicus DEM (European Space Agency Sinergise, 2021). The green square marks the location of the trench (HUTc-1) in Deng et al. (1996). (d) Mapping and interpretations from this study with faults marked in red.

north-dipping normal fault (F4) (Figures 4c, 5a and 5b). This normal fault is interpreted to be the fault that forms the hinge graben mentioned in Avouac et al. (1993). The reverse fault F1 dips 53° and has ∼2 m vertical displacement; the reverse fault F2 dips ∼45° and has ∼0.78 m vertical displacement. The reverse fault F3 has a variable dip angle from 39° to 73° and penetrates the surface with a ∼0.3 m high free face (Deng et al., 1996). Combining the trench log with the thermal luminescence dating results from the offset sediments, Deng et al. (1996) suggest only two Holocene earthquakes are identified and fault F3 had ruptured during the 1906 Manas Earthquake.

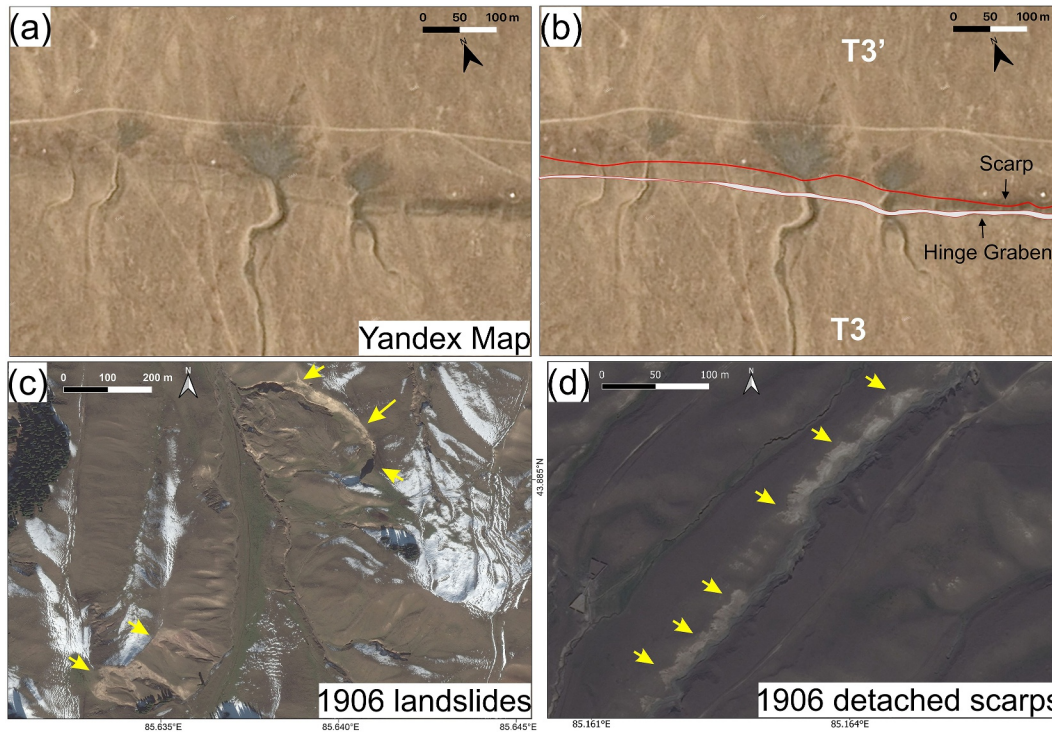

Figure 5. (a) and (b) Zoomed-in Yandex Map (0.4 m resolution) view of the Hutubi Fault scarps (in red) and hinge graben across T3 and T3′ shown in Figure 4a. (c) The landslides near Shichang, shown in Bing Maps (0.2 m resolution), possibly caused by the 1906 Manas Earthquake (d) A possibly detached scarp, sliding to the southeast, caused by the 1906 shaking near the Shiaonanguo River shown in Bing Map. Locations of (c) and (d) are labeled in Figure 3a.

Fresh fault scarps are found on the youngest terrace T1 with a single-step and no beveling, indicating they are single-event scarps (Avouac et al., 1993; Zhang, Deng, Xu, Peng, et al., 1994). Nevertheless, their heights as measured from topographic profiles vary in the literature, Avouac et al. (1993) reported the average height of T1 fault scarps is 0.83 ± 0.15 m whereas Zhang, Deng, Xu, Peng, et al. (1994) and Deng et al. (1996) reported the heights to be only 0.2–0.3 m. Zhang, Deng, Xu, Peng, et al. (1994) presented trench data across the fault scarp on terrace T1 showing one fault plane dipping 25–30° to the south with underlying strata displaced only about 0.35 m. Although there is variation in height, both the lower scarps (0.3–1.1 m) at the foot of the composite scarps on T3 and the fresh <1 m scarps on T1 are all compatible with slip in the 1906 Manas Earthquake.

3.2.2. Eastern Terraces of the Manas River

The northward-flowing Manas River is located between the Tugulu Anticline and the Manas Anticline (Figure 3a). On the eastern bank of the main Manas River, there are six major terrace levels recognized, T6 to T1 from high to low, with terraces T5 and T6 being intensively deformed by the two faults that have a ∼2 km interval between each other (Gong et al., 2015) (Figure 6). The western extension of the HTF is present at terrace T5 of the Manas River and has produced 3–5 m high scarps on it near 86.1251°E, 44.1698°N (Avouac et al., 1993; Gong et al., 2015) (Figure 6c). The Manas Fault (MNF), bounding the north side of the Manas Anticline, terminates on terrace T6 and has produced 7–10 m high scarps on both T5 and T6 near 86.1417°E, 44.1883°N, north of the HTF scarps (Avouac et al., 1993; Gong et al., 2015) (Figure 6). Some previous studies do not associate these two scarp series with the 1906 Manas Earthquake due to the highly-degraded scarp surfaces and the lack of scarp continuity to the younger terraces (Avouac et al., 1993; Zhang, Deng, Xu, Wu, et al., 1994); however, trenching data from this site are interpreted to show the possible influence of the 1906 Manas Earthquake. Deng et al. (1996) excavated a trench (MTc-4), at the MNF scarp on T5, and they revealed no surface rupture but the top three layers, including soil and gravels, are warped, suggesting recent deformation. Gong et al. (2015) reported a very fresh surface rupture of the MNF within the T5 surface at 86.1329°E, 44.1885°N (site MNS2); however, they did not

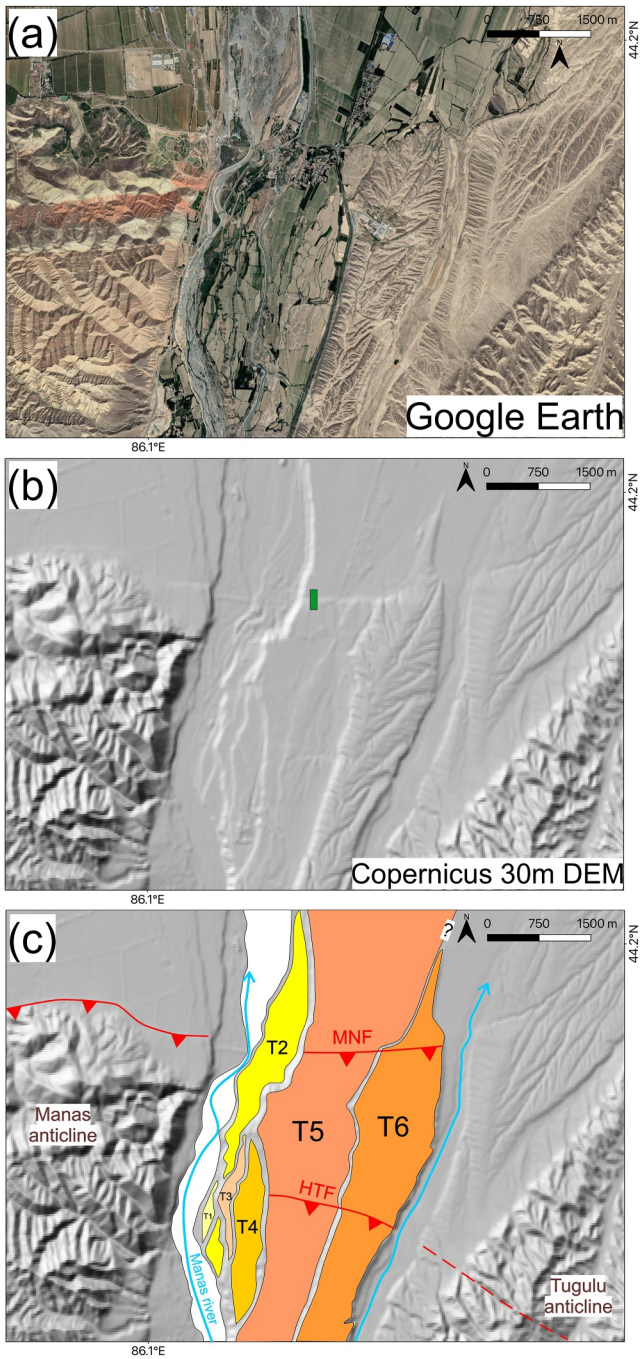

Figure 6. Two series of fault scarps (in red) along the Manas River (Region B in Figure 3) between the Tugulu and Manas Anticlines shown in (a) optical satellite imagery in Google Earth Map (0.2 m resolution) in 2019 and (b) shaded topographic relief from the Copernicus 30-m DEM (European Space Agency Sinergise, 2021). The green rectangle marks the location of the trench (MTc-4) in Deng et al. (1996). (c) Mapping and interpretations from this study. MNF: Manas Fault; HTF: Hutubi Fault.

associate it with any historical event, and we further suggest this rupture is probably an artificial scarp since it is at the edge of a small man-made trail. Apart from trench MTc-04 and site MNS2, the other trenches or outcrops observed by Deng et al. (1994, 1996) and Gong et al. (2015) in this region do not show recent surface rupture.

3.2.3. Aweitan Gulley (the Middle Part of the Manas Fault)

Zhang, Deng, Xu, Peng, et al. (1994) reported a ~300 m long fault scarp at the Aweitan Gulley which is a 4–5 m high composite scarp with the latest vertical offset around 0.6 m (Profile A-A′ therein). A trench (MTc-3) dug at this site indicated this scarp is the product of an underlying fault (Deng et al., 1996). However, there is no description in that literature of the precise locations of the Aweitan Gulley, the scarps and the trench. According to the previous mapping from Zhang, Deng, Xu, Wu, et al. (1994) and Deng et al. (1996), we infer the site to be south of Aweitan village near 85.987°E, 44.198°N, which is ~7 km southeast of the Shihezi Airport (Figure 3a), where a series of fresh scarps are visible in satellite imagery (Figure 7). Quite a few unnamed gullies in this region now contain water dams, quarries, or roads that have obscured or degraded the previously identified fault scarps. We suggest the most likely scarps mentioned in Zhang, Deng, Xu, Peng, et al. (1994), Zhang, Deng, Xu, Wu, et al. (1994) might be either in the west of the Aweitan Gulley at 85.9543°E, 44.2053°N or on the Aweitan terrace at 85.9757°E, 44.1987°N, which has now been destroyed by quarry construction (Figure 7).

3.2.4. Western Terraces of the Jingou River

The northward-flowing Jingou River (also called the Huoerguos River) cuts throw the E-W trending Huoergous Anticline and the Huoergous Fault (Figure 3a). Prominent fault scarps along the Huoergous Fault can be easily recognized for ~2.5 km on the western side of the Jingou River, and displace all the five terrace levels that are present (Avouac et al., 1993; Pang et al., 2021; Zhang, Deng, Xu, Peng, et al., 1994). The terraces are labeled T5–T1 from high to low in this study (Figure 8). The morphology of the Huoergous Fault scarps is similar to the HTF scarps as having a hinge graben at the top and showing distinct lower scarps at the bottom of the main scarp that is interpreted as resulting from the most recent surface rupture. The average heights of fault scarps on terraces T5 and T4 are ~11 m and 4.6 ± 0.5 m, respectively, and both with hinge graben (Avouac et al., 1993; Pang et al., 2021). On terrace T3, the average scarp height is 4.0 ± 0.4 m (Pang et al., 2021). A secondary fault on T3, and a distinct step at the bottom of the T3 composite scarps have similar heights measured at 0.9 m by Avouac et al. (1993) and 0.5–0.7 m by Li et al. (1992) and Zhang, Deng, Xu, Peng, et al. (1994). These <1 m vertical offsets are similar to those found at the Hutubi River terraces and the freshness (outlined by turf and rodent holes) of them observed in the field suggests they are less than hundreds of years old (Avouac et al., 1993; Zhang, Deng, Xu, Peng, et al., 1994). The composite scarps measured on terrace T2 are 2.8 ± 0.3 m high with a hinge graben at the top (Pang et al., 2021). No scarp data were reported from terrace T1 since there is a hydrological infrastructure built on it (Figure 8a). Deng et al. (1996) excavated a trench (HOTc-1) in the youngest terrace of the Jingou River that should be located on the terrace T1 mapped in this study, although no precise location was provided. A reverse fault dipping 40° to the south was found in this trench and the top sediment layer, dated at ~6,900 cal. year B. P., has been warped by the latest earthquake event which is interpreted to be the 1906 Manas Earthquake (Deng et al., 1996).

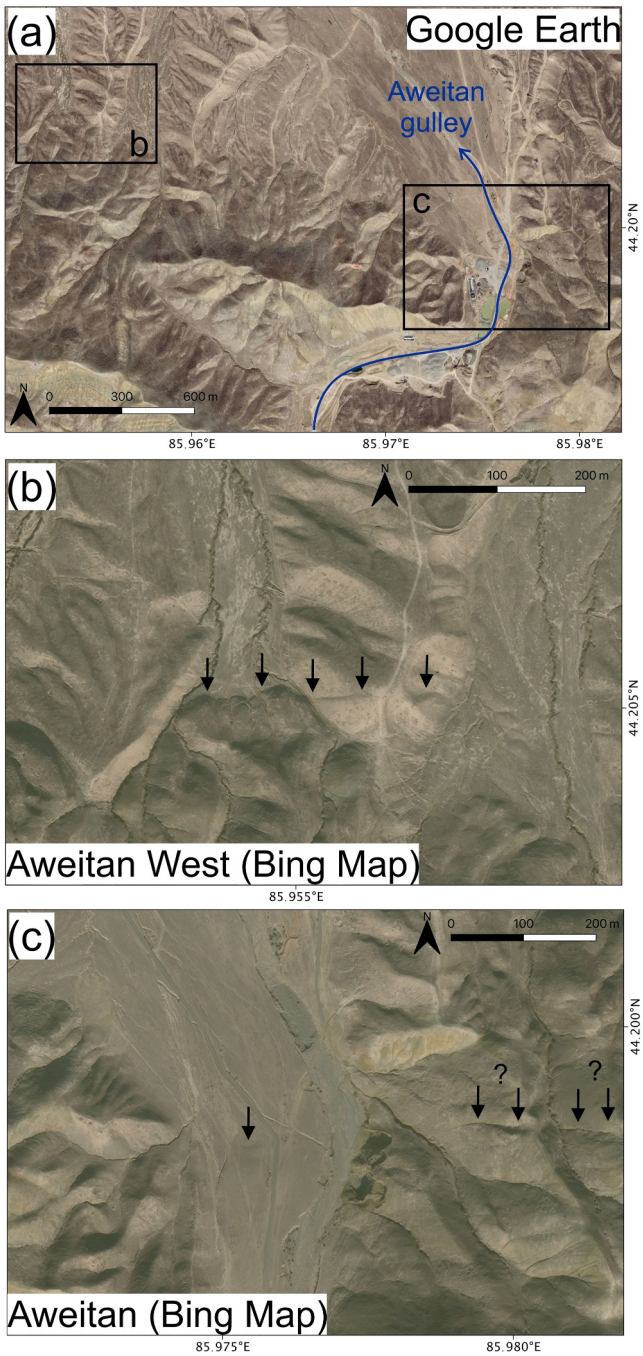

Figure 7. (a) The likely 1906 surface ruptures (pointed by black arrows) at the Aweitan Gulley (Region C in Figure 3) shown in optical satellite imagery with two specific sites shown in (b) and (c). A quarry infrastructure can be seen in the 2019 Google Earth Map (0.2 m resolution) in (a) but Bing Map (0.2 resolution) in (c) caught the landscape before the exploitation.

3.2.5. The Northern Hills of the Borohoro Shan

Previous surveys have shown that the most damaged area during the 1906 Manas Earthquake extends for ~40 km along the range front of the BRS from the Manas River to the Shiaonangou River (Seismological Bureau of Xinjiang, 1985) (Figure 3a). Most of the ruptures in this region are gravity-triggered landslides, fissures and detached scarps instead of compressional ruptures (Bai & Fang, 1981; Zhang, Deng, Xu, Peng, et al., 1994). In this study, "landslides" are defined to be U-shaped mass wasting with obvious headscarps and sliding bodies. "Fissures" are shaking-triggered tensional cracks that do not display offset. Unlike the scarps that show obviously hanging-wall and foot-wall offsets within the stratigraphy, "detached scarps" are gravity-triggered linear scarps that only offset the loose surface materials, like soil or loess, but not the bedrock (Zhang, Deng, Xu, Peng, et al., 1994).

From the Manas River to the Ningjia River, the type of surface ruptures is mostly large landslides with their crowns up to hundreds of meters wide (Zhang, Deng, Xu, Peng, et al., 1994) (Figures 3a and 5c). From the Ningjia River to Nuiquanzi (Figure 3a), most ruptures are fissures longer than 100 m with a depth of 0.1–0.2 m and a width of 0.3–0.4 m developed along the gulleys (Zhang, Deng, Xu, Peng, et al., 1994). Nevertheless, it is difficult to recognize these fissures from the imagery nowadays, probably due to their relatively small sizes and post-earthquake erosion. Some smaller landslides with tens of meters sliding and 1–2 m-high head scarps are also recognized from the Ningjia River to Nuiquanzi (Zhang, Deng, Xu, Peng, et al., 1994). From the Jinguo River to the Shiaonangou River, most ruptures are detached scarps developed along the secondary loess layer on the sides of gulleys (Zhang, Deng, Xu, Peng, et al., 1994) (Figures 3 and 5d). These detached scarps are usually tens to hundreds of meters long and 0.5–1 m high with a SE sliding direction (Zhang, Deng, Xu, Peng, et al., 1994) (Figure 5d). Some trenches were dug across the detached scarps and they showed no fault nor offset within the bedrock but some fissures within the secondary loess layers, indicating they are shaking-induced mass wasting (Seismological Bureau of Xinjiang, 1985; Zhang, Deng, Xu, Peng, et al., 1994). Bai and Fang (1981) mentioned several 2.5 m dextral displacements along the right-stepping en echelon reverse cracks in this region but we have no information about their locations.

A likely fault scarp at the northern hills of the BRS is reported by the Institute of Geophysics, SSB & Institute of Chinese Historical Geography, (1990), who include a photo showing the ~2 m-high scarp in the south of Bo'ertonggu, but without giving a precise location and we could not identify this scarp from modern satellite imagery (Figure 3a). A north-dipping backthrust is visible in the landscape immediately north of the BRS rangefront at longitude ~85.5 E (Figure 3a; G. Hu et al., 2021). This backthrust scarp is interpreted as the surface expression of a bedding-parallel back-thrust interpreted within upper Eocene deposits from a seismic reflection line at longitude ~86 E. Although this fault has moved in the Holocene, the available age control suggests the last surface displacement was more than 2,000 years ago, and so it does not appear to have ruptured in the 1906 earthquake. As it is not clear how far eastwards the backthrust extends, we have not marked it on our cross section (Figure 3b).

3.2.6. Anjihai-Dushanzi Anticline

Along the Anjihai Anticline (Figure 3a), no fresh fault scarps have been reported in the previous studies. Between the Halaande Anticline and the Dushanzi Anticline, left-stepping en echelon faults are recognized on the river terraces (Figure 3a), indicating some dextral fault movements in this region (Avouac et al., 1993; Deng

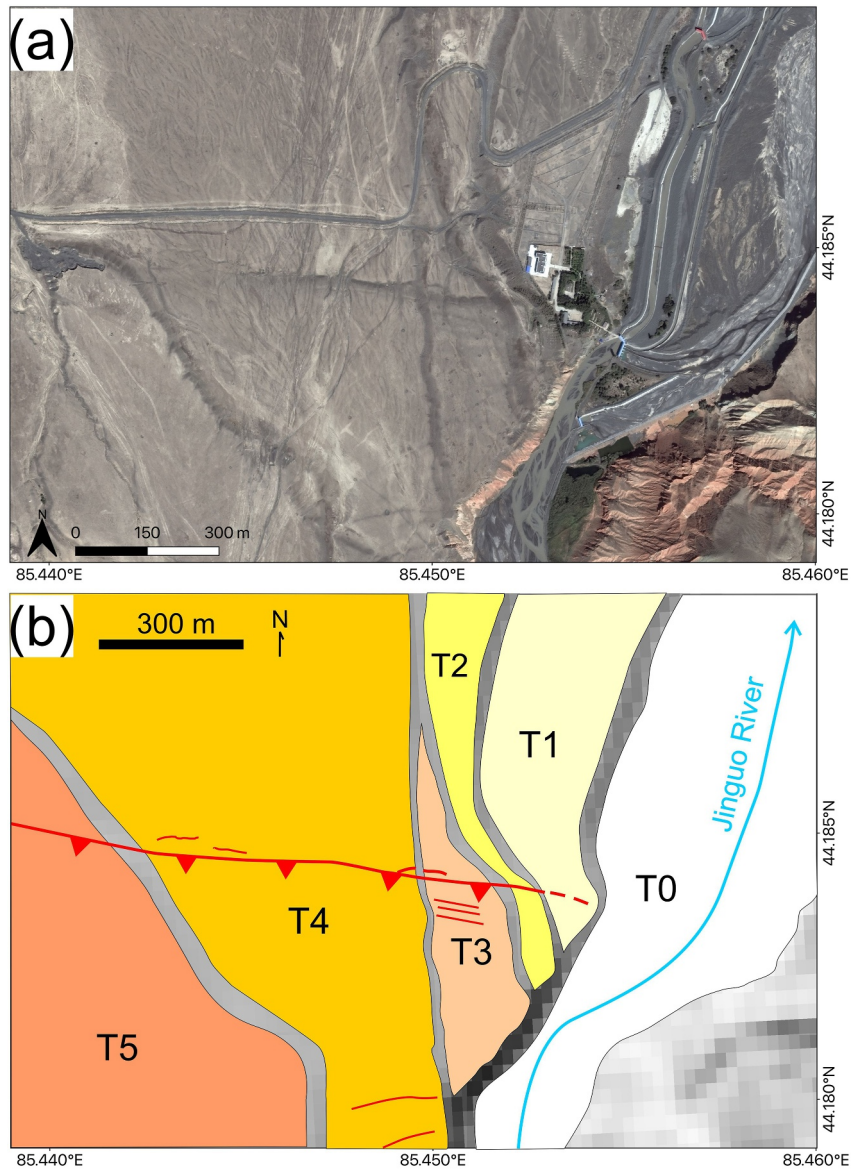

Figure 8. The Huoerguos Fault scarps in the western bank of the Jinguo River (Region D in Figure 3) shown in optical satellite imagery from Bing Map (0.2 m resolution). (b) Mapping and interpretations with faults marked in red based on the shaded topographic relief from the Copernicus 30-m DEM (European Space Agency Sinergise, 2021). The trench (HOTc-1) was dug into the youngest terrace which is now obscured by infrastructure (Deng et al., 1996).

et al., 1991). The trench data along the Anjihai Anticline and across those en-echelon faults indicate two Holocene earthquakes in the intervals 6–8 ka and 3–5 ka respectively, but no earthquake evidence could be found within the last 3,000 years (Deng et al., 1991) (Figure 3a). On the western bank of the Kuitun River, which cuts through the Dushanzi Anticline, several <3 m-high fault scarps are found on the high-level terraces (Deng et al., 1996; Su et al., 2018). However, the trench data collected from these Dushanzi scarps also imply the thrust here has not ruptured the surface for at least the past 800 years (Figure 3a) (Li et al., 2012; Su et al., 2018). These all indicate the 1906 Manas Earthquake did not cause surface rupture from Anjihai to Dushanzi Anticlines. In sum, the surface ruptures of the Manas Earthquake can only be observed between the east of the Anjihai River and the west of the Hutubi River, which is 120–140 km long (Figure 3a).

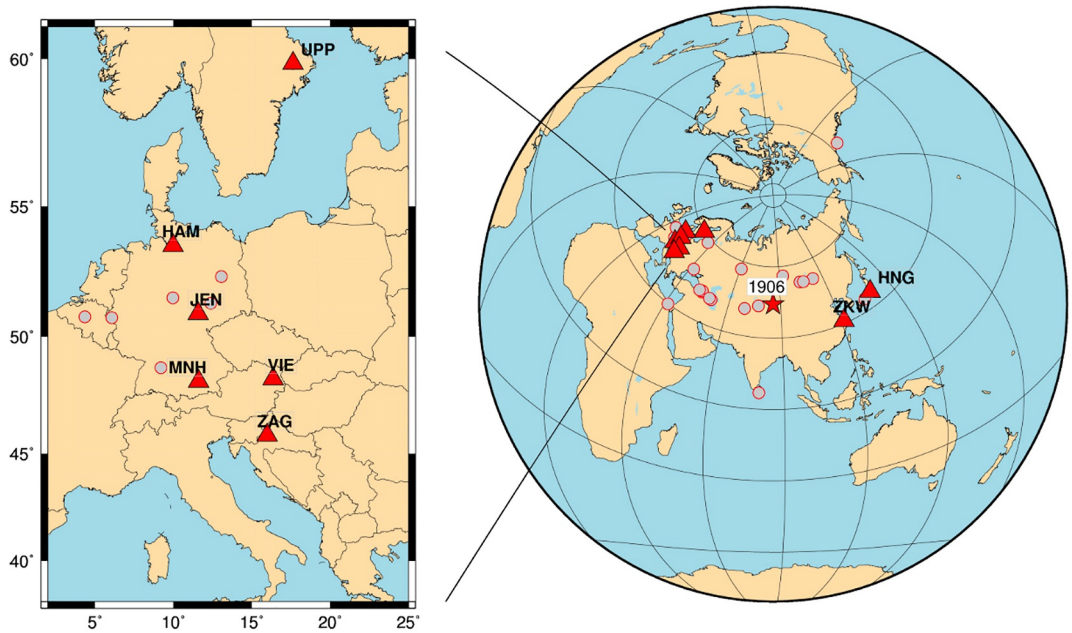

Figure 9. Station distribution map for the 1906 Manas Earthquake. Red star shows the epicenter location of this event; Gray circles show the seismic stations, from which the bulletins, including different phase arrival times, were available; Red triangles show the stations from which seismic records were obtained.

3.3. Previously Estimated Magnitudes

A summary of the previously reported magnitudes is shown in Table 1 with the corresponding references and methods. The largest magnitudes for the 1906 Manas Earthquake were estimated to be Ms 8.3 by Richter (1958) and Molnar and Deng (1984) and lower magnitudes were also reported to be M 8 (Bai & Fang, 1981; Gu, 1983; ISC, 2021), Ms 7.9 (Gutenberg & Richter, 1954), Mw 7.8 ± 0.2 (Storchak et al., 2013), and M 7.7 (Deng et al., 1996; Institute of Geophysics, SSB & Institute of Chinese Historical Geography, 1990; Lu et al., 2018; Wang et al., 2004; Yang et al., 1998, 2002; Zhang, Deng, Xu, Peng, et al., 1994; Zhou et al., 2003). Some even suggested the magnitudes were only Ms 7.3 (Abe, 1988) or Ms 7.2 (Abe & Noguchi, 1983) from the implication that the surface wave magnitudes inferred from the seismograms of 1897–1912 events might be systematically overestimated. However, Avouac et al. (1993) disagreed with these low magnitudes from the comparison with other better-estimated historical events. Avouac et al. (1993) further added their field survey results with certain assumptions to calculate the magnitude as Ms 8 ± 0.2, based on the surface rupture length of 150 km and the assumed fault slip, dip and depth of 3.5 ± 2 m, 45°S and 15–40 km respectively, which is the most detailed implication of the fault geometry. It is also worth noticing that Chinese studies after 1990 all use Ms 7.7 as referring to the Institute of Geophysics, SSB & Institute of Chinese Historical Geography (1990) or Zhang, Deng, Xu, Peng, et al. (1994).

3.4. Seismological Analysis and Earthquake Mechanism

3.4.1. Data Acquisition

We collected 14 seismic records of the Manas earthquake from 8 stations to relocate the epicenter, construct the focal mechanism and re-estimate the magnitude. The station distribution is presented in Figure 9. The majority of the seismograms were collected from seismic stations located in Europe, due to better preservation of records and easier accessibility. Considering the epicentral distance (about ~5,000 km), the European stations altogether can be considered as a large aperture distant seismic array, which allows stacking of the traces to improve the signal-to-noise ratio (Kulikova & Krüger, 2015). Seismograms from seismic station HNG, Tokyo, Japan and Chinese station ZKW (ZiKaWei) were added to the data collection providing observations from different azimuths. (The HNG seismogram was only available as image without scale, which is thus excluded from magnitude calculations in the following step). The 1906 Manas Earthquake has been recorded by analogue seismic instruments with the

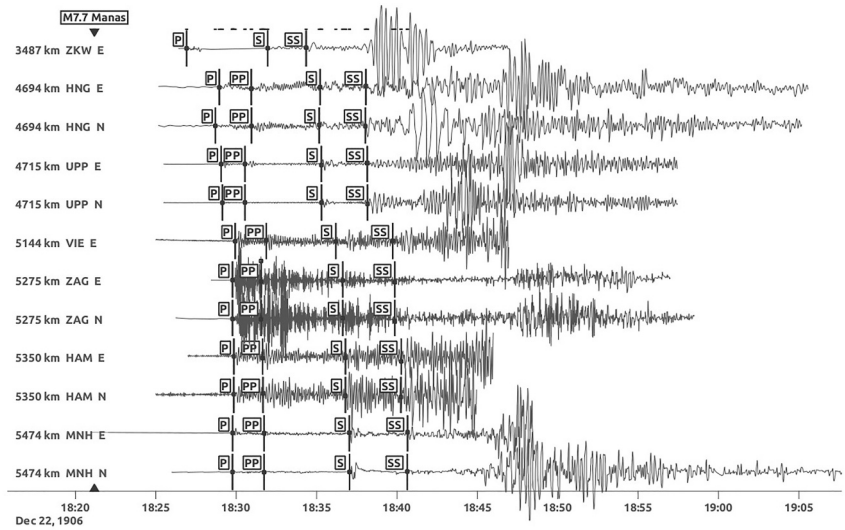

Figure 10. Digitized seismic records of the 1906 Manas Earthquake from the 8 seismic stations (Figure 9). The curvature was corrected using the method in Cadek (1987) and the traces are normalized. The dominant P, PP, S and SS phases are marked accordingly.

seismograms existing either as original paper recordings or as reproductions on microfilm, or as photographs in books. For further processing, the analogue seismograms were digitized manually using the path tool of GIMP (GNU Image Manipulation Program) (Kimball et al., 2013) and the technique described by Kulikova (2016) and Ou et al. (2020). Prior to digitization, the scanned seismograms were calibrated using the known scan resolution and the time marks printed on the original records. Pixel coordinates extracted from the traced waveform were converted into physical displacement values using the graphical amplitude scale of the record and the available instrument magnification constants. The seismograms used in this study were selected based on record completeness, waveform clarity, and the availability of instrument parameters. To minimize digitization errors, ambiguous waveform segments (e.g., overlapping traces or damaged parts of the record) were excluded, and the consistency of phase arrivals was verified across stations. The uncertainty of the digitization is mainly controlled by the scan resolution, the thickness of the original trace, and the preservation state of the historical records.

Examples of digitized seismic waveforms of the Manas Earthquake are presented in Figure 10. The records show a clear P phase arrival followed by an impulsive S wave, especially on the N component of the European stations. In addition, both direct P and S phases are followed by dominant larger amplitude arrivals, which are attributed to the surface reflections PP and SS accordingly.

3.4.2. Epicenter Relocation

The limited number of available stations and the poor azimuthal coverage introduce considerable uncertainty into the epicentral location based solely on waveform data, as only 14 seismograms are available and most stations are located in Europe. To improve the stability of the location procedure, arrival time information from historical seismic bulletins was additionally incorporated. In total, 24 local and teleseismic bulletins were consulted and combined with the arrival times measured on the digitized seismograms. Altogether, 58 onset times of identified phases and 21 arrival-time differences were used in the relocation.

The epicenter was determined using the program HYPOSAT (Schweitzer, 2001, 2012). Travel times were calculated using the CRUST 5.1 model for the crustal structure in the source region and the AK135 global velocity model for the mantle part of the ray paths (Kennett et al., 1995; Mooney et al., 1998). No additional local modification of the crustal structure for the BRS region was introduced. Considering that the data set consists primarily of teleseismic long-period arrivals and includes substantial observational uncertainties associated with historical records, the standard CRUST 5.1 regional model was considered sufficient for the relocation.

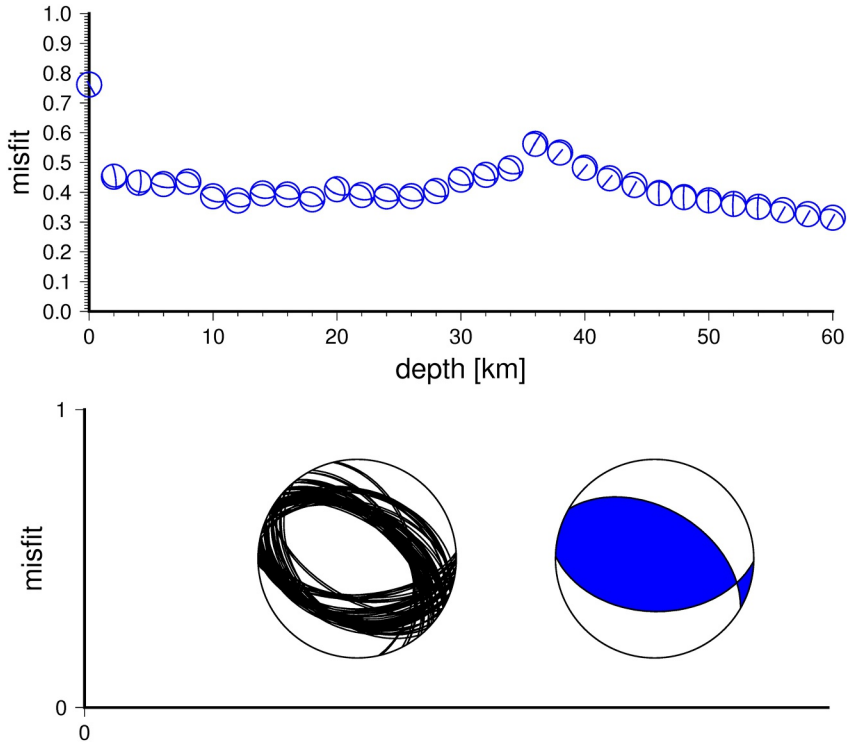

Figure 11. Focal mechanism determination of the 1906 Manas Earthquake. The top panel shows the mechanism determination for different tested depths; the bottom panel shows the 5% best solutions and the solution with the minimum misfit. The misfit values represent the difference between observed and synthetic waveforms obtained from forward modeling of seismic waveforms for different focal mechanism parameters and depths. The misfit is defined as misfit $= \frac{1}{N}\sum_{i=1}^{N}\left|\frac{A_i^{obs}-A_i^{syn}}{A_i^{obs}}\right|$, where A_i^{obs} and A_i^{syn} are the observed and synthetic amplitude ratios, respectively.

Three epicentral solutions were obtained from the inversion (Table 2 and Figure S1 in Supporting Information S1):

1. 44.09°N, 85.16°E using arrival times picked from the digitized waveforms,
2. 44.04°N, 84.61°E using bulletin arrivals only, and
3. 43.96°N, 84.93°E using a combination of both data sets.

All three solutions are consistent with each other and place the epicenter approximately 100 km southwest of Manas County. Because no reliable depth phases (e.g., pP or sP) could be identified, the focal depth could not be independently resolved from arrival-time data. The hypocentral depth was therefore fixed at 20 km for the HYPOSAT relocation procedure in order to stabilize the epicentral inversion, representing a reasonable seismogenic depth for a large intracontinental earthquake in the Tien Shan region. This fixed depth applies only to the hypocentral relocation. In a separate analysis (Section 3.4.3), waveform amplitude-ratio and focal-mechanism misfit tests were performed for a range of source depths in order to evaluate which depth ranges are most compatible with the observed long-period waveforms.

Table 2
Relocated Epicenter Locations for 1906 Manas Earthquake

Number	Location type	Origin time (hh:mm:ss.s)	Latitude (°N)	Longitude (°E)	Depth (km)
1	Waveforms only	18:21:08.3 ± 2.0	44.093 ± 0.6691	85.158 ± 0.3850	20.00-Fixed
2	Bulletins only	18:21:09.6 ± 3.9	44.039 ± 0.6560	84.608 ± 0.6011	20.00-Fixed
3	Preferred location	18:21:10.6 ± 1.9	43.958 ± 0.5214	84.926 ± 0.2954	20.00-Fixed

3.4.3. Focal Mechanism

The amplitude ratios comparison method was used for focal mechanism determination of the 1906 Manas Earthquake (Kulikova & Krüger, 2015; Ou et al., 2020). Amplitude ratios of different phases (body waves only: P, PP, S and SS phases were used) were compared in a grid search procedure to the synthetic records amplitude ratios for different focal mechanisms to determine the best amplitude ratios fit. All combinations of strike, dip and rake ($0° < \text{strike} < 360°$, $0° < \text{dip} < 90°$, $-180° < \text{rake} < 180°$, with 2° step for all) for a double couple source were tested considering a point source. Grid search was performed over different test depths from 0 to 60 km with a 2 km step (Figure 11). The minimum misfit, corresponding to the best, was observed for the combination strike/dip/rake: 96°/46°/70°. Although the minimum misfit defined 96° strike, the 5% best solutions varied in strike between 96° and 116°, which would mean the strike is likely to be around 106 ± 10°. The minimum misfit for dip angle is at 46° from the best solutions varied between 46° and 56°, implying the earthquake has likely occurred on a steeply dipping fault (51° ± 5°). Based on the overall tectonic regime of the region we suggest the ruptured fault plane is the south-dipping plane (see Figures 3 and 11). Unfortunately, with the available limited data set, the method proved rather insensitive to source depth. The tested depth range shows a broad misfit minimum between approximately 10 and 30 km, with the lowest overall misfit at ∼18 km (Figure 11). However, the minimum is relatively broad and therefore does not tightly constrain the focal depth. Instead, the analysis indicates a preferred middle-crustal depth range, while substantially deeper mantle sources are disfavored because they do not reproduce the observed long-period surface-wave amplitudes adequately. This preferred depth range is consistent with the fixed 20 km depth used for the HYPOSAT epicentral relocation (Section 3.4.2).

3.4.4. Magnitude Estimation

We determined magnitudes m_B and M_S using the amplitudes and periods of body and surface waves from seismic bulletins and digitized waveforms. Moment magnitude M_W was also determined based on waveform modeling. Broadband body wave magnitude m_B was determined using the Gutenberg and Richter (1956) formula corrected for geometric spreading and distance-dependent attenuation (Bormann et al., 2013). For the case of the 1906 Manas Earthquake, the broadband body wave magnitude m_B is especially important since the seismic instruments operating at that time mostly had limited dynamic range and were frequently not able to record the full amplitude of surface waves. Moreover, the period of the instruments was more suitable for recording the shorter period of body waves than surface waves. The amplitudes and period data used for m_B estimation are presented in Table S1 in Supporting Information S1. It is subdivided into two parts showing the data found in seismic bulletins and the values measured on digitized waveforms. Although the amplitude values from bulletins and waveforms differ, even for the same station (possibly due to the unknown method used to convert from mm on paper to μm of displacement by the analysts at that time), the average magnitude for all stations remains the same and equals to m_B 7.4 ± 0.3. The estimation of surface wave magnitude was based on the maximum amplitudes of surface waves using the "Moscow-Prague 1962 formula" (Kárník, 1962). Results of M_S estimation are presented in Table S2 in Supporting Information S1, with separation for bulletins and waveforms amplitudes as well, resulting in M_S 7.9 ± 0.2. This value is similar to Ms 8.0 ± 0.2 in Avouac et al. (1993), supporting that Ms 7.2–7.3 is likely underestimated whereas Ms 8.3 is likely overestimated (Table 1).

After the focal mechanism was determined with amplitude ratio comparison, forward waveform modeling was used to estimate the moment magnitude Mw. For the fixed focal mechanism, the synthetic seismograms were simulated for different Mw and compared in a grid search with the observed data, in order to determine the best waveform fit. For this procedure, only true-scale seismograms (full scans, no microfilms) with precisely known instrument parameters were used. In our case, these were the seismograms from the European stations. The best waveform fit was observed for an average magnitude Mw 7.7 with ±0.2 magnitude deviation for different stations. This agrees with the Mw 7.8 ± 0.2 in Storchak et al. (2013) and further implies the Mw 7.95 from the latest ISC-GEM catalog could be the upper bound (ISC, 2021). A magnitude of ∼Mw 7.7 for a thrust earthquake suggests a rupture width of 20–40 km (Blaser et al., 2010). This rupture width is consistent with a mid-crustal seismogenic depth and supports the choice of a fixed hypocentral depth of 20 km in the HYPOSAT relocation (Figure 11).

An approximate source time duration of the earthquake can be directly estimated from the P-wave record. The majority of the seismograms obtained for this study were recorded on seismic stations in Europe (about ∼5,000 km away from the epicenter) on ground displacement proportional Wiechert horizontal pendulums with

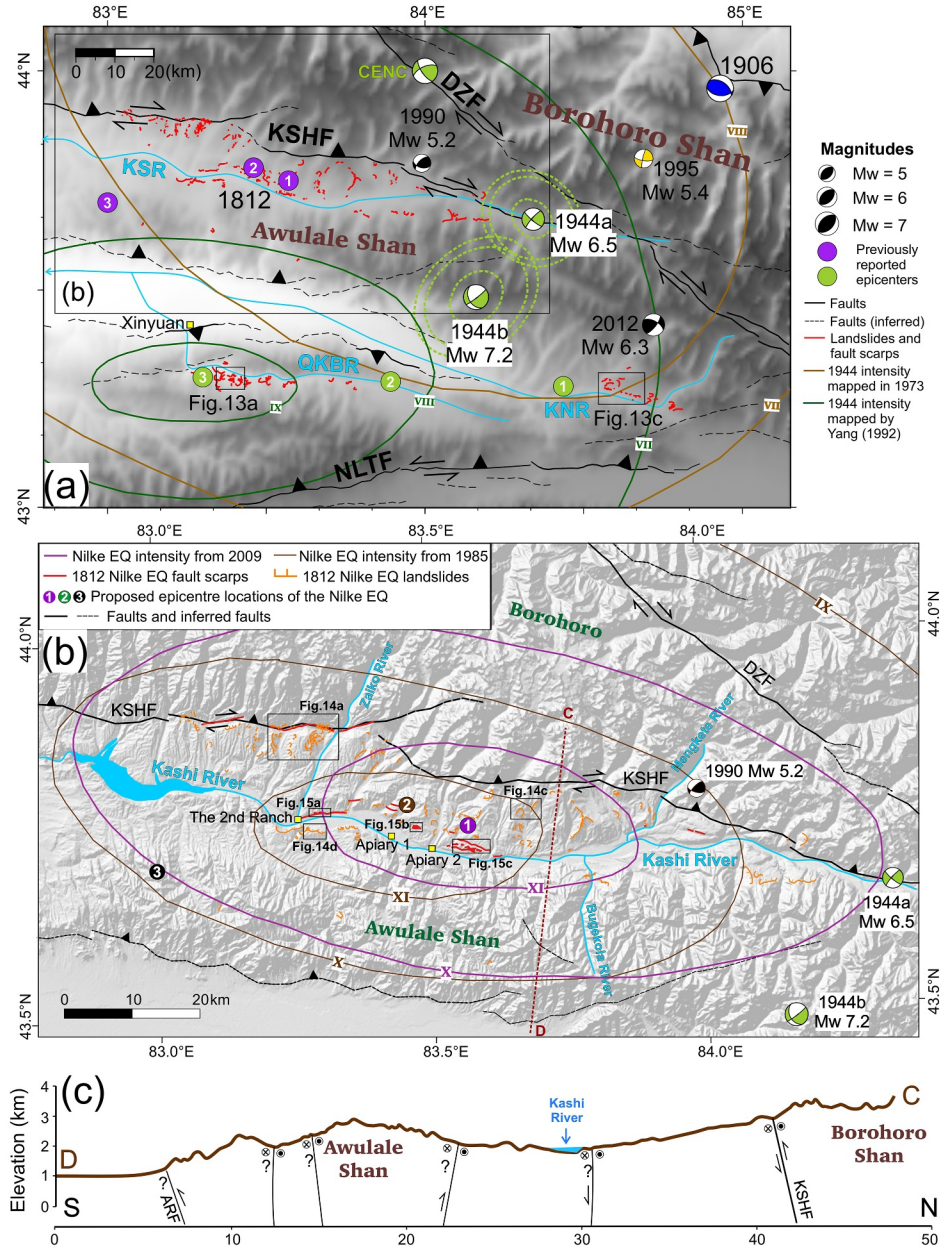

Figure 12. (a) Overview of the southern Borohoro Shan (BRS) with epicenters of the 1944 (light green), 1906 (blue) and 1812 (purple) earthquakes. The 1944 Xinyuan Earthquake double-event focal mechanisms and epicenters relocated by this study are shown with the error ellipses in green dashed lines. Color-filled circles are the previously reported epicenters with the numbers described in the caption of Figure 2. The likely earthquake-induced landslides are marked in red. Focal mechanisms of earthquakes from 1976 to June of 2021 with Mw ≥ 5 are displayed and labeled based on the GCMT data (Dziewonski et al., 1981; Ekström et al., 2012) except for the 1995 Mw 5.4 event (in yellow) which is from Sloan et al. (2011). Isoseismal maps for the 1944 event are marked in light brown for the version mapped in 1973 and in dark green for the version mapped in 1992, both in New Chinese Intensity Scale. Xinyuan Town is annotated by the yellow square. KSHF: Kashihe Fault; DZF: Dzhungarian Fault; NLTF: Nalati Fault; KSR: Kashi River; QKBR: Qiakebo River; KNR: Kunes River. (b) Overview of the 1812 Nilke Earthquake with ESRI shaded relief imagery. Isoseismal maps from Yang et al. (1985) and Yin et al. (2009) are shown in brown and purple respectively and labeled in New Chinese Intensity Scale. Color-filled circles are the previously reported epicenters with detailed descriptions in the caption of Figure 2. Landslides and fault scarps possibly related to the 1812 event are labeled in orange and red respectively. Rivers are delineated in light blue. Faults are in black (Zelenin et al., 2021). (c) Seismotectonic section with along the profile C-D in the southwestern BRS interpreted by this study inspired by the mapping database in http://www.ngac.org.cn/Map/Document?guid=EC7E1A7A79E71954E0430100007F182E. ARF: Awulale Range Front Fault.

only slightly different instrument responses. To estimate the source time duration from the European stations, P-waves were aligned and stacked together, to improve the signal-to-noise ratio (see Figure S2 in Supporting Information S1), it should be noted that P-wave duration was measured on the horizontal E-component since the preferred vertical component was not available). The overall maximum P-wave source duration was ∼37–40 s, which would produce ∼110–120 km rupture considering the case of unilateral rupture and taking the average rupture velocity as 2.9 km/s. Empirical scaling relations suggest a magnitude Mw 7.7–7.8 for this rupture length (Blaser et al., 2010; Wells & Coppersmith, 1994).

3.5. Seismogenic Faulting

The strike (96°) and rake (70°) of our modeled focal mechanism suggest predominantly thrusting parallel to the northern margin of the BRS. The epicentral location indicates that it nucleated beneath the northern Borohoro range, though we do not have a direct constraint on nucleation depth, and with a relatively steep dip of ∼51° to the south. The surface ruptures, however, are found along the northern margin of a series of folds ∼10 km north of the BRS range front, with a total length of ∼125 km for the three ruptured segments.

We first exclude the Anjihai-Dushanzi Fault to be the responsible fault for the 1906 event since most of the reported epicenters are far away from it and the trenching data indicate the Anjihai-Dushanzi Fault has not ruptured at least in the past 800 years (Figure 3a) (Deng et al., 1991; Li et al., 2012; Su et al., 2018). According to what we have observed, analyzed and compiled for the 1906 Manas Earthquake, the responsible fault for this event should be the SJT. Moreover, we notice that definitions of the SJT vary in different literature, which could cause confusion and has complicated the debate on the responsible fault (Deng et al., 1996; Z. Hu, Yang, et al., 2021; Lu et al., 2018; Stockmeyer et al., 2014; Zhang, Deng, Xu, Peng, et al., 1994). In this study, we define the SJT to be the major thrust closest to the northern BRS and the others (e.g., the Hutubi-Houergous Fault) as the branches of the SJT (Figure 3b).

Interpretations of seismic reflection data suggest there are two layers of detachments under the Qingshuihe and Qigu Anticlines, with the shallower one (∼7 km at depth) being a branch of the SJT that propagates to the north and penetrates to the surface as the Hutubi-Houergous Fault (Figure 3b) (Lu et al., 2018; Stockmeyer et al., 2014; Wang et al., 2004). Since this branch starts to dip down to the south at ∼22° ± 5° under the Qigu Anticline (Lu et al., 2018; Stockmeyer et al., 2014), it can reach a depth of >15 km beneath the BRS, which is consistent with our compilation for the depth of the 1906 event (Table 1). However, the dip of ∼22° does not match the dip of 51° ± 5° from our modeled focal mechanism. Therefore, we suggest the 1906 Manas Earthquake is likely to have ruptured on the SJT at depth beneath its connection to the Hutubi-Houergous splay, with slip then transferred onto that splay to reach the surface to the north (Figure 3b). The absence of deformed Quaternary strata and the unclear geomorphic expression of the SJT fault trace (Avouac et al., 1993; Zhang, Deng, Xu, Peng, et al., 1994; Zhang, Deng, Xu, Wu, et al., 1994) suggests that slip did not propagate to the surface along the range-front fault. Ground deformations along the range-front appear to be related to gravitational movements, rather than tectonic faulting, although 2-m high fresh fault scarps were reported by the Institute of Geophysics, SSB & Institute of Chinese Historical Geography, (1990), that we cannot confirm, and without precise reporting of location. The phenomenon of surface ruptures occurring on fault splays at distance from the main range-front fault has also been found in other historical events such as the Tabas-e-Golshan earthquake in Iran and the Chi-Chi earthquake in Taiwan, and is a common feature of active fold-thrust belts (Berberian, 1982; Lee & Chan, 2007; Walker et al., 2003). This could be the result of complex upward propagation and splaying within an imbricate thrust system, whereby slip transmitted along the basal décollement re-emerges at shallower foreland ramps (Hughes & Shaw, 2014; Stockmeyer et al., 2014). Our modeled focal mechanism of the 1906 event is similar to the 2016 Mw 6.0 Hutubi Earthquake which is suggested to occur on the Hutubi-Houergous Fault (Figure 3), but with different dips albeit both epicenters are close to the SJT (Lu et al., 2018). This might further support that the 1906 event is associated with a major structure that has different geometry and could host larger-magnitude earthquakes than the Hutubi-Houergous Fault itself only. However, we could not exclude the possibility that the Hutubi-Houergous Fault is the only ruptured fault for the 1906 event and that it has a steeper dipping angle in the west of the Qigu Anticline.

From earthquake scaling relations (Wells & Coppersmith, 1994; Wesnousky, 2008), the dip of ∼51°, the magnitude Mw ∼ 7.7 and the ∼125 km surface rupture length of the 1906 event yield a total slip of ∼7–9 m. Considering the absence of large surface displacements, this implies that most of the surface deformation is accommodated either by folding or dissipated at depth (Long et al., 2025).

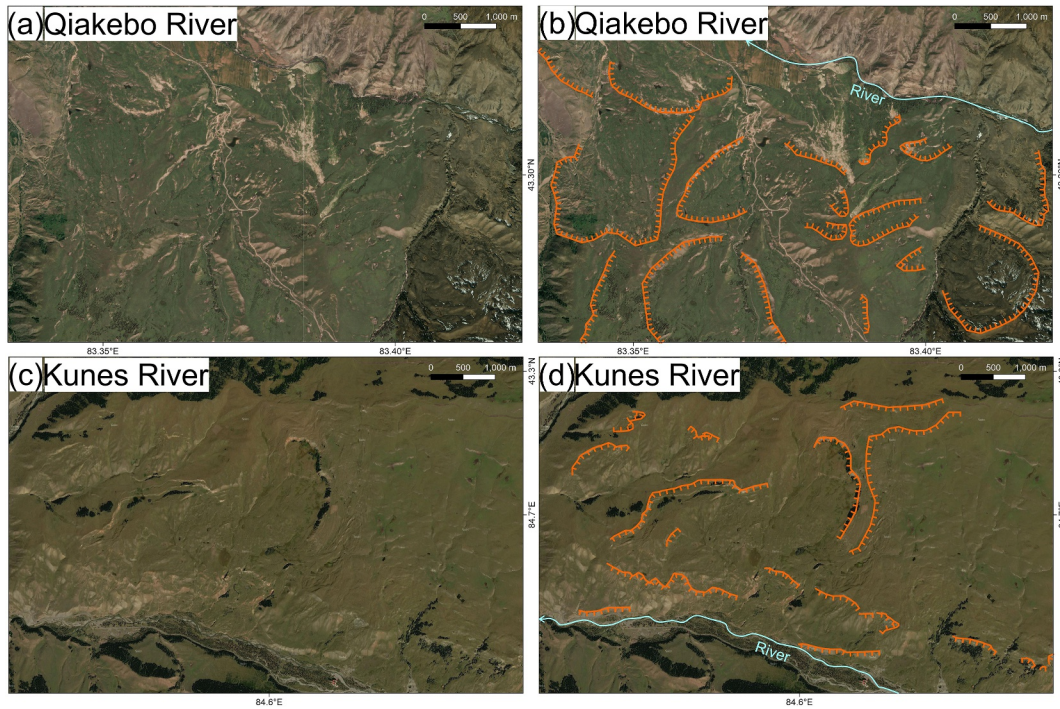

Figure 13. (a) Bing Map (0.3 m resolution) and (b) Yandex Map (0.4 m resolution) showing landslides possibly caused by historical earthquakes found in the southern Borohoro Shan along (a) the Qiakebo River and (b) The Kunes River. Locations are labeled in Figure 12a. The landslides are mapped with their crown in orange lines in (b) and (d).

4. The 1944 Xinyuan Earthquake

4.1. Background and Macroseismic Data

The 1944 Xinyuan Earthquake occurred on 10th March (local date) in the southern BRS. There are two versions of the isoseismal map with quite different coverage and inferred epicenters (Figure 12a). The earlier version was made in 1973 and depicted the area of intensity VII and VIII and an inferred epicenter at 44°N, 84°E which is inside the BRS and is cataloged in the CENC database with a recorded magnitude of Ms 7.3 (Figure 12a) (Z. Yang, 1992 and CENC). A later version was proposed by Yang (1992) who identified the likely most damaged area with an intensity of IX in the southeast of Xinyuan Town with prominent landslides and an inferred epicenter at 43.3°N, 83.3°E (Figure 12a) (Z. Yang, 1992). However, based on the USGS earthquake catalog, the epicenter of the 1944 Xinyuan Earthquake is a double event that has a smaller Mw 6.9 foreshock at 43.28°N, 84.43°E, which occurred ten minutes before the Mw 7.1 main shock at 43.29°N, 83.89°E (Figures 2 and 12a).

4.2. Seismological Analysis, Surface Ruptures and Discussion

We performed a seismological analysis for the 1944 Xinyuan Earthquake using exactly the same approach as for the 1906 Manas Earthquake described in Section 3.4 (Figure 2). Therefore we skip redundant information about the methods in this section. We re-estimated the magnitudes and relocated the hypocenter using 26 digitized seismograms from 11 stations and bulletin information from over 60 stations. (Detailed figures of the analysis are included in the supplementary material.) Our results confirm the 1944 Xinyuan Earthquake was a double event but with different locations of epicenters from those reported by USGS and the previous studies. The Mw 6.5 ± 0.3 foreshock (1944a) occurred at 22:03:43 UTC on 9th March. The epicenter was located at 44.66°N and 84.34°E. The Mw 7.2 ± 0.2 main shock (1944b) occurred 9 min later (22:12:59 UTC) at 43.48°N, 84.16°E (Table 3). Both events occurred at 24-km depth (Figure 12a). The epicentral uncertainties obtained from the HYPOSAT relocation are ±0.13° in latitude and ±0.12° in longitude for the foreshock (1944a), and ±0.15° and ±0.19° for the main shock (1944b). These uncertainties correspond to spatial errors of several tens of kilometers and are illustrated by the error ellipses shown in Figure 12a.

Table 3
Relocated Epicenter Locations

Event	Origin time (date, hh:mm:ss.s)	Latitude (°N)	Longitude (°E)	Depth (km)
1906	December 22nd, 18:21:10.6 ± 1.9	43.958 ± 0.5214	84.926 ± 0.2954	20 Fixed
1944a	March 9th, 22:03:43.29 ± 1.2	44.662 ± 0.1278	84.341 ± 0.1221	24
1944b	March 9th, 22:12:59.31 ± 1.4	43.484 ± 0.1465	84.161 ± 0.1906	24

Yang (1992) interpreted landslides clustered along the Qiakebo River (now called Qiapu River), which are covered by trees growing after 1944, as resulting from the 1944 Earthquake (Figures 12a and 13a, 13b). Nevertheless, other places in the southern BRS also have clustered landslides such as those spreading along the KSR, which are usually inferred to result from the 1812 Nilke Earthquake (Feng, 1990, see Section 5), and those

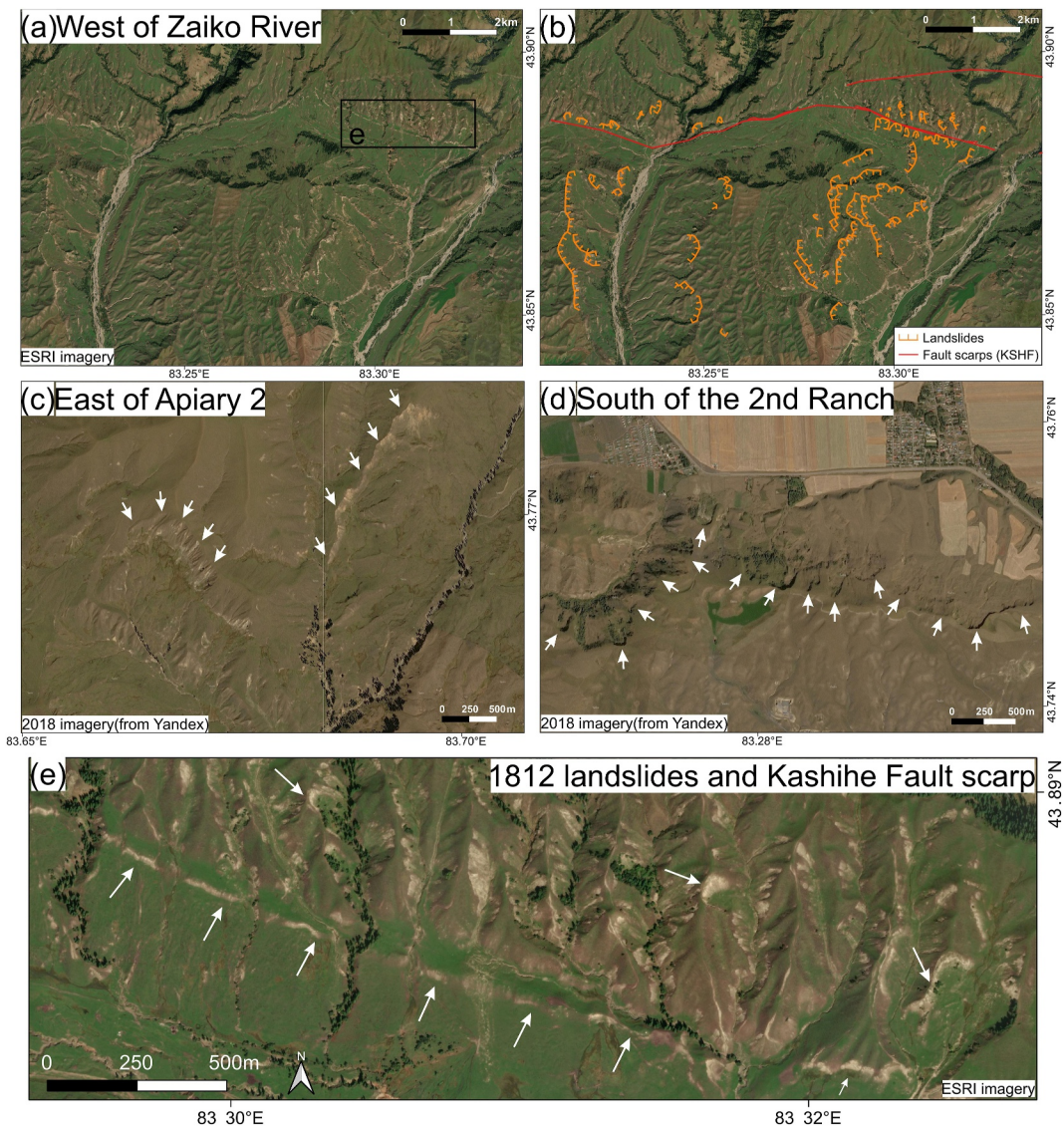

Figure 14. (a) ESRI optical satellite imagery (0.3 m resolution) showing the likely 1812 landslides and fault scarps in the west of the Zaiko River with annotations in (b). (c) and (d) Optical satellite imagery from Yandex Map (0.4 m resolution) showing the likely 1812 landslides in the east of Apiary 2 and the south of the 2nd Ranch. (e) The Kashihe Fault trace with a prominent fault scarp in the west of the Zaiko River, which has been visited and measured by Wu et al. (2020). Fault scarps and landslide crowns are pointed by white arrows. Locations of each panel are labeled in Figure 12b.

along the Kunes River (KNR) that we identify here for the first time (Figures 13c and 13d). It is worth noticing that none of these landslide clusters fit well with our relocated epicenters for the 1944 double-event although the KNR landslides could align with the NW-SE fault strike inferred from the 1944b focal mechanism (Figure 12a). According to our relocated epicenters, the landslides along the Qiakebo River should be the least likely caused by the 1944 events since they are located furthest from the epicenters. Further field investigation and more precise chronological constraints are needed to examine the timing and cause of the landslide clusters along the Qiakebo River.

The relocated foreshock (1944a) epicenter and its focal mechanism (strike/dip/rake = 220/70/-10) are consistent with the Kashihe Fault trace and its right-lateral strike-slip component (Figure 12a) (Feng, 1987; Wu et al., 2020). Thus, it is possible that the 1944a event occurred on the Kashihe Fault or one of its branches, although the DZF still remains a candidate for the responsible fault considering its similar kinematic and its proximity with the 1944a event (Shen et al., 2003). Our re-estimated focal mechanism for the 1944a event is similar to the focal mechanism estimated by CENC which is also of mainly strike-slip type, but the inferred fault strike and epicenter location from CENC is more consistent with the DZF (Figure 12a). Our relocated epicenter of the main shock (1944b) is inside the Awulale Shan with a focal mechanism (strike/dip/rake = 50/80/-50) indicating an oblique slip consisting of normal and strike-slip components, either with right-lateral slip on an NW-SE trending and SW-dipping fault or on a near-vertical left-lateral fault trending NE-SW. No prominent fault trace could be recognized near the 1944b epicenter except the inferred range front structure of the Awulale Shan and some elusive fault branches within the mountains (Figure 12a). Considering the Awulale range front structure should be a reverse fault, it is less likely to be the ruptured fault for the 1944b event, which is dominated by normal components. There could be other, unidentified, strike-slip faults that are responsible for the 1944b earthquake. The 2012 Mw 6.3 events with similar focal mechanisms of mostly strike-slip movement are present near the 1944b event (Figure 12a) (Dziewonski et al., 1981; Ekström et al., 2012; Fang et al., 2014), again indicating such fault kinematics are dominating within the eastern Awulale Shan. Higher-resolution imagery, in situ surveys and palaeoseismic trenching would be needed to reveal more tectonic and structural characteristics of the Awulale Shan.

5. The 1812 Nilke Earthquake

5.1. Background and Macroseismic Data

The Nilke Earthquake occurred in the evening on 8th March 1812 local time near Nilke County (Figures 1 and 2). The magnitude of this earthquake was estimated to be Ms 8 and it caused at least 58 fatalities and over five thousand deaths of livestock, mainly due to landslides (China Earthquake Administration, 1971; Institute of Geophysics, SSB & Institute of Chinese Historical Geography, 1990; Yang et al., 1985). A detailed survey of the surface ruptures of the Nilke Earthquake began in the 1970s and these ruptures are dominated by landslides and are distributed along the KSR, especially on its northern bank (Feng, 1990; Wu et al., 2020; Yang et al., 1985; Yin et al., 2001, 2006) (Figure 12b). The first isoseismal map of the 1812 Nilke Earthquake was made by Yang et al. (1985) based on contemporary Qing Dynasty damage records, and the size and distribution of earthquake-induced landslides. The intensity reached XI on the New Chinese Intensity Scale from Zaiko River to the west of Bugekola River and reached VI near Yining City (Figures 1b and 12b) (Yang et al., 1985). However, Yin et al. (2009) re-evaluated the distribution of surface ruptures from modern airborne photos and relocated the isoseismal contours ∼15 km to the east of the 1985 one, suggesting the area of XI intensity extended from the east of the Zaiko River to the west of the Mengkete River (Figure 12b). The epicenter of the earthquake was reported to be near 43.7°N, 83.0°E by China Earthquake Administration (1971) but it has been relocated to 43.78°N, 83.46°E by Yang et al. (1985) and 43.75°N, 83.57°E by Yin et al. (2009) according to their isoseismal maps (Figure 12b). Despite the discrepancy in the epicenter and intensity coverage, they all suggest the most severe ground shaking appeared in the Apiary area, and had a broadly east-west elongation (Figure 12b). Based on the intensity and the distribution of surface ruptures, the 1812 Nilke Earthquake has been implied to have occurred on the Kashihe Fault (Feng, 1987, 1990; Wu et al., 2020; Yang et al., 1985; Yin et al., 2002). However, reverse fault scarps and lateral offsets are scarce whilst numerous landslides and normal fault scarps can be observed in the most damaged area, which is ∼10 km south of the Kashihe fault trace (Figure 12b).

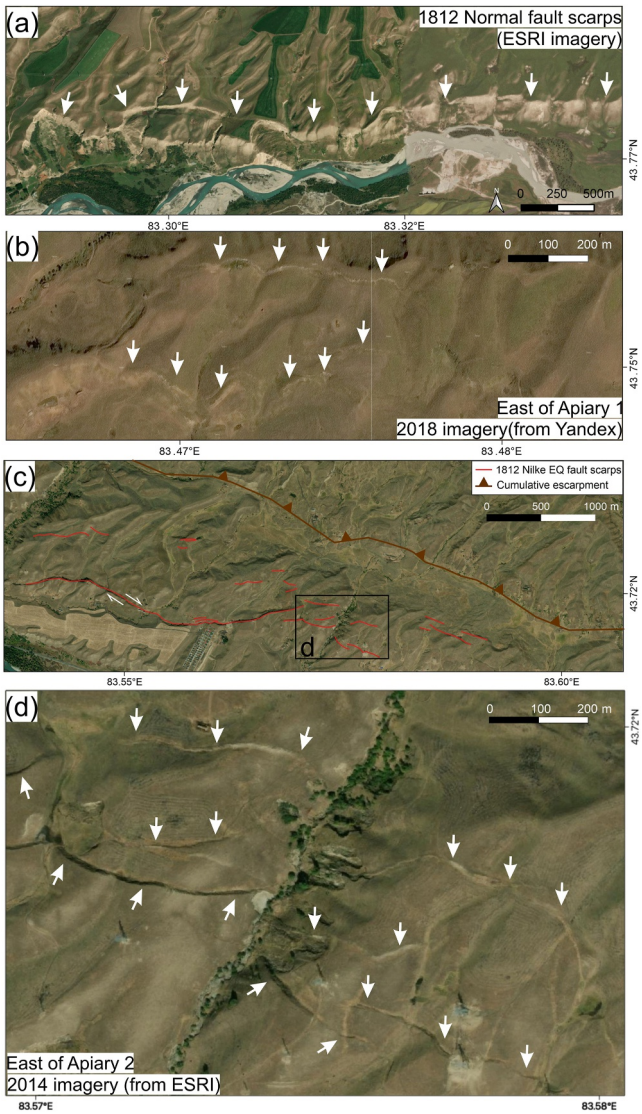

Figure 15. (a) A large normal fault scarp near the 2nd Ranch, visited by Yin et al. (2002) and Wu et al. (2020), shows ~15 m of vertical offset and a laterally offset channel, likely produced by the 1812 event. (b) The likely 1812 normal scarps mentioned in Feng (1990) and Yin et al. (2002) in the east of Apiary 1. (c) Reverse, strike-slip and normal fault scarps near Apiary 2. The ~70 m high cumulative reverse scarp measured by Wu et al. (2020) is marked in brown. The 4-km-long Z-shape fault scarp (red) with dextral movements is trenched and described by Feng (1990). (d) Grabens that are likely formed in the 1812 event by the normal scarps. A profile of this graben has been illustrated in Feng (1990). Locations of each panel are labeled in Figure 12b.

5.2. Surface Ruptures

The surface ruptures of the 1812 Nilke Earthquake can be categorized into four main types: landslides, normal fault scarps, fissures, and reverse fault scarps. We note that the term 'surface ruptures' for the 1812 event is used here in a broader descriptive sense to encompass all ground deformation features documented in previous studies (Yin et al., 2001, 2006), and that this differs from its strict seismological definition. The most widely distributed are the landslides. Thousands of landslides have been observed with 365 of them having widths larger than 500 m with the widest ones reaching 5 km (Yin et al., 2001) (Figures 14b–14d). The previous studies have identified earthquake-induced landslides based on their clustered distribution, and also on the steepness of their main scarps and the sliding surfaces, with inferred earthquake-induced landslides having shallower dips and occurring on gentle hill slopes of only 6°–19° (Yin et al., 2001, 2006). The density of landslides decreases noticeably away from the high-intensity region (Feng, 1990; Yang et al., 1985; Yin et al., 2001, 2006) (Figure 12b).

The second commonly observed ruptures are normal fault scarps, mostly distributed in the XI isoseismal area (Figures 12b and 15). While the origin of individual scarps remains uncertain where field evidence is lacking, as some may represent trailing edges of landslides or riverbank collapses, the overall pattern of normal fault scarps in the region is broadly supported by field observations reported in previous studies (Feng, 1990; Wu et al., 2020; Yin et al., 2001, 2006). Ninety-two sites have been identified, with 28 of them also showing right-lateral displacements (Yin et al., 2006). These normal fault scarps mostly dip to the south although several north-dipping ones are also recognized (Figure 15c) (Feng, 1990; Yin et al., 2002, 2006). The majority of these normal faults are formed by E-W striking faults with several of them having listric geometry with steep (60–80°) slopes at the top that are shallow toward the bottom (Feng, 1990; Yin et al., 2002, 2006). East of Apiary 2, ~200-m-wide grabens are also found to be bounded by the normal faults (Figure 15c). Compared to the landslides, these normal fault scarps have good linearity and their extension is not constrained by topography (Yin et al., 2006). Furthermore, trenching results show some of these normal faults only cut through the thick loess and soil layer at the surface but not the bedrock underneath (Feng, 1987). The vertical offsets of these normal fault scarps are 2–10 m with the largest offset up to 15 m with right-lateral offsets of 1.5–4 m (Feng, 1990; Yin et al., 2002) (Figures 15a, 15b and 15d). The third commonly found ruptures are tensional fissures that do not have offsets and are mostly N-S striking, which means they tend to be perpendicular to the fault scarps (Yin et al., 2002, 2006). Nevertheless, there is a lack of information on the locations of these fissures in the literature.

Only 12 reverse fault scarps were reported to be produced by the Nilke Earthquake but only four of them were described in detail, and no precise locations were provided (Feng, 1990; Yin et al., 2002). These four reverse scarps are in the east of Apiary 2 which are ~2 m high with scarp surfaces facing to the north and with underlying faults dipping 56°–62° to the south as constrained by paleoseismic trenching, although no precise scarp nor trench locations were provided (Feng, 1990; Yin et al., 2002). There is also a ~70 m high cumulative reverse escarpment in the east of Apiary 2 (Wu et al., 2020) (Figure 15c). In the southwest of this cumulative escarpment, there is a ~4 km long S-shape north-facing fault scarp which is 2–15 m high with 2.5–4 m right-lateral displacements (Feng, 1990) (Figure 15c). From the previous trenching data and the field outcrop, this north-facing scarp is a steeply-dipping dextral-slip fault with the 1812 surface ruptures cutting the top loess layer (Feng, 1990; Wu et al., 2020). West of the Zaiko River, there is a series of south-facing scarps at the range front and they are considered to be the Kashihe Fault trace (Figures 14a, 14b and 14e) (Wu et al., 2020).

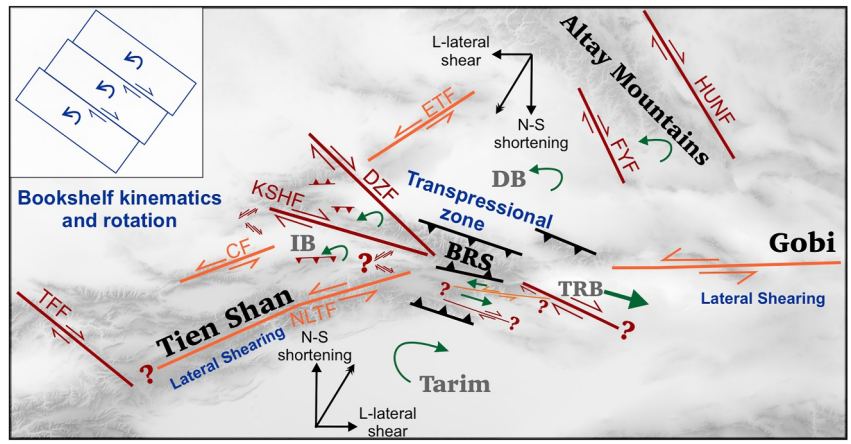

Figure 16. Simplified crustal deformation kinematics around the Borohoro Shan (BRS). Main left-lateral strike-slip faults are displayed in orange. Main right-lateral faults and other smaller faults are displayed in brown with the fault kinematics labeled. Black arrows show the shortening and shearing directions. Green arrows show the crustal/block motion with respect to the BRS. Types of deformation are annotated in blue with a model in the upper right showing bookshelf deformation. NLTF: Nalati Fault; CF: Chilik Fault; ETF: East Tacheng Fault; TFF: Talas-Fergana Fault; KSHF: Kashihe Fault; DZF: Dzhungarian Fault; FYF: Fuyun Fault; HUNF: Har-Us-Nuur Fault; DB: Dzhungarian Basin; IB: Ili Basin; TRB: Turfan Basin.

Landslides inferred to be from the 1812 earthquake are widespread on both the northern and southern sides of these scarps (Yin et al., 2001, 2002) (Figures 14b and 14e).

We digitized the previously reported 1812 surface ruptures with our own mapping results in Figure 12. Although we could not locate all the previously mapped ruptures due to a lack of precise locations given in the literature, most of the large landslides and the prominent normal and reverse fault scarps could still be recognized from the present-day satellite imagery. However, fissures and other reverse fault scarps are not easily distinguished due to the image resolution and the long-term erosion. According to our compilation, the majority of the Nilke Earthquake surface ruptures are located north of the KSR but they generally have distances from the main Kashihe Fault trace (Wu et al., 2020; Zelenin et al., 2021), with the prominent inferred ruptures within the highest-intensity area distributed in a zone 7–10 km south of the main Kashihe Fault trace (Figure 12b). WNW of the highest intensity area, oblique-slip ruptures are identified along the main Kashihe Fault trace (Figure 14a,b, e).

5.3. Earthquake Magnitude and Mechanism

The estimated magnitude of the 1812 Nilke Earthquake is Ms 8.0–8.1 based on intensity-magnitude relationships (China Earthquake Administration, 1971; Yang et al., 1985). However, recent seismological investigation of several of the large earthquakes of the early to mid-20th century have indicated that the magnitudes derived from seismic intensities may be overestimated (Kulikova & Krüger, 2015; Ou et al., 2020), with the seismology-derived magnitudes in broad agreement with geologically derived estimates from rupture length and slip distribution (Klinger et al., 2011; Ou et al., 2020). Pre-instrumental earthquake magnitudes derived from intensity information may, therefore, be similarly overestimated (e.g., Feng et al., 2020; Middleton et al., 2015), with the discrepancy likely arising from the use of Gutenberg surface wave magnitude in the formulation of the intensity-magnitude relationship (Ou et al., 2020). If that is the case, the approximate Mw for the Nilke earthquake would be ∼7.7.

The surface rupture of the Nilke Earthquake could extend up to 124 km (Yin et al., 2009), though from our own mapping, the length of surface ruptures is approximately 100 km (Figure 12b). Yang et al. (1985) calculated the depth of the Nilke Earthquake to be ∼25 km from the isoseismal distribution (Liu, 1961), which is consistent with the nearby recent earthquake depths of 20–40 km (ISC, 2022a). Using the scaling relationship from Wells and Coppersmith (1994) and Blaser et al. (2010), the 100–124 km surface rupture length yields a magnitude of Mw 7.5–7.7 and Mw 7.6–7.8, respectively. Using the scaling relationship from Wesnousky (2008), this surface rupture length yields a magnitude of Mw 7.3–7.4 and Mw 7.9–8.0 for strike-slip and reverse faulting respectively. A magnitude of Mw 7.7–8.1 is estimated from estimates of the rupture area, assuming a depth of 20–40 km, length

of 100–124 km, average displacement of 7.5 m from the mean offset of the scarps (Yin et al., 2006) and a fault dip of 45°–75° (Aki, 1966; Kanamori, 1977; Wu et al., 2020). In sum, the 1812 Nilke Earthquake magnitudes implied from both scaling relationships and the rupture area align in the range from Mw 7.3–8.0.

Yang et al. (1985) suggested the ruptured fault plane strikes 280° and dips 68° to the north with a rake of ∼95°, indicating this is a mainly reverse faulting event. The regional N-S convergence and the behavior of the Kashihe Fault are consistent with the reverse mechanism of the Nilke Earthquake. Our interpretation of the observed ruptures and other surface deformation is that the 1812 Nilke Earthquake more likely had components of both right-lateral and reverse faulting and that it could have a focal mechanism similar to the 1990 Mw 5.2 event near the Kashihe Fault (Figure 12b). A number of the faults within this southern rupture zone show right-lateral displacements, which highlights the strike-slip motion of the responsible faults. The majority of the 1812 ruptures are found occurring on another fault or branches that are ∼10 km distant in the south of the recently mapped main Kashihe Fault (Wu et al., 2020; Zelenin et al., 2021), with an alignment that is parallel to it (Figures 12b and 12c). The 1812 Nilke Earthquake likely ruptured both the Kashihe Fault and another splay to the south of it.

The Awulale Shan and its surrounding regions are accommodating not only the N-S shortening but also a rotation with westwards extrusion, inferred from the fact that they are bounded by a dextral strike-slip fault in the north and a sinistral strike-slip fault in the south (Figures 12a and 16). Several historical events show strike-slip mechanisms within the Awulale Shan (see Section 5.2), also suggesting the overall oblique slip on the faults. The fault pattern and geometry could be complex in this area with predominantly oblique slip during earthquakes, which is likely able to produce the diverse types of surface ruptures of the 1812 event. The normal component of the 1944b event might also result from the complicated kinematics of crustal deformation within the Awulale Shan. Grützner et al. (2019) have suggested a zigzag pattern of strike-slip faults, with right-lateral faulting on NW-SE planes and left-lateral faulting on NE-SW planes, which are accommodating the shortening in the west of the Ili Basin (IB) (Figure 16). Different scales of this zigzag fault pattern might also exist in the eastern IB with the same fault kinematics observed from the historical events in the Awulale Shan (Figures 12a and 16). However, it is difficult to map the faults in this region merely from the remote sensing imagery. Field surveys and the associated in situ investigations will be essential to unravel the detailed seismogenic structures in the southwest BRS.

6. Discussion

Our investigation of the 1812 Nilke, 1906 Manas, and 1944 Xinyuan earthquakes has helped to refine our knowledge of likely source parameters of all three events. The 1906 Manas Earthquake likely ruptured a steeply-dipping thrust at depth beneath the BRS margin, but with a slip that was transferred across a decollement to rupture the surface for a distance of 125 km along the Huoerguos, Manas, and Tugulu anticline segments (see Section 3.5)(Figure 3). The 1906 earthquake possibly nucleated at the lower western corner of the fault plane and ruptured unilaterally eastwards. This is also seismologically supported by lower than average m_B magnitudes in Europe and a high m_B value observed at station ZKW in China (see Table S1 in Supporting Information S1).

The 1944 Xinyuan Earthquake is confirmed to be two earthquakes closely spaced in time and location, with an Mw 6.5 earthquake being followed by an Mw 7.2 earthquake ∼25 km to the southwest (Figure 12a). Both events have similar strike-slip mechanisms, with right-lateral faulting on an NW-SE plane, or left-lateral faulting on a NE-SW plane. The causative faults of the 1944 events remain ambiguous; while the section of the right-lateral Kashihe Fault southeast of the 1812 rupture is a plausible candidate, the DZF and other regional structures cannot be excluded on the basis of current evidence.

The 1812 earthquake possibly involved oblique reverse and right-lateral slip along the Kashihe Fault, and also a splay from it that projects to the surface near the KSR (Figure 12c). Using scaling relationships we estimate a magnitude of in the range of Mw 7.3–8.0, with most of the estimation methods yielding Mw > 7.5 (see Section 5.3) (Figure 12a).

Several recent studies have drawn attention to the apparent over-estimation of magnitude from intensity measurements for Chinese earthquakes of historical and early instrumental periods (Feng et al., 2020; Kulikova, 2016; Kulikova & Krüger, 2015; Middleton et al., 2015; Ou et al., 2020). The discrepancy has been interpreted to result from the use of Gutenberg surface wave magnitude in the intensity-magnitude relationship (e.g., Ou et al., 2020), though may also relate to bias in intensity measurements from densely populated basin regions that may be

susceptible to enhanced shaking. Our results from the BRS agree with the pattern, with the 1906 Manas Earthquake having a redefined moment magnitude of Mw 7.7 that is substantially smaller than previously stated magnitudes from intensity X. The better-constrained rupture length of the 1812 Nilke Earthquake also suggests that the likely upper-bound magnitude does not reach M 8+, as previously estimated from intensities.

In the northern range front of the BRS, the surface topography only reflects the structures less than 10 km deep in the crust as inferred from the wavelength of anticlines and the seismic-reflection profile (Figure 3). The likely coseismic slip for the 1906 Mana Earthquake is less than 1 m, observed from the fault scarps among the terraces. Both the seismic depth and the fault slip indicated solely by the surficial features are less than the seismological re-estimated results for the 1906 event as >15 km of depth and ∼7–9 m of slip. This indicates that surface geomorphology could disguise the sub-surface structural complexity (Mackenzie et al., 2016). For example, the seemingly shallow faults may have a large down-dip extension or may be connected with hidden deeper structures like the case of the 2016 event (Lu et al., 2018; Wang et al., 2019). Furthermore, in some cases, rupture starting at the deeper part of the fault would not propagate upwards, which prohibits the surface rupture but retains the seismic risk in the shallow unruptured portion (Z. Hu, Li, et al., 2021). The example of the 1906 Manas Earthquake provides another lesson that surface topography may not fully reflect the depth extent of seismogenic faulting and that additional information, such as seismic-reflection profiles, is needed to help interpret the seismotectonics. In the southern range front of the BRS, the complex strike-slip fault system could pose great seismic hazards, but it is less identifiable from the surface geomorphology. More in situ investigations are needed to help reveal the active faulting in this region.

In terms of local earthquake hazards, an important feature of all three earthquakes is the widespread association of landslides. Landsliding was responsible for much of the destruction and loss of life in, for example, the 1920 Haiyuan, 2005 Kashmir and 2008 Wenchuan Earthquakes (Daniell et al., 2017; Nowicki Jessee et al., 2020). Thousands of people died due to the collapse of loess cliffs, where they resided, and the landslides caused by shaking during the 1556 Huaxian Earthquake in central China (Feng et al., 2020). Many of the landslides possibly triggered by the earthquakes in the BRS occurred in relatively low-relief regions in areas of thick loess cover too, with identification aided by the study of tree shapes and additional radiocarbon dating Yang, 1988, 1992). The widespread and damaging landslide points to the potentially damaging effects that might be expected in future large earthquakes. Despite the difficulties in distinguishing seismically-induced landslides from those triggered by other factors, such as the collapsible structure and low shear strength of loess, the landslides associated with the three known earthquakes form distinct clusters. The identification of landslide clusters may provide an efficient means of paleoseismic investigation in such mountainous and loess-covered landscapes, particularly as the ruptures may fail to reach the surface, or be hard to identify. The landslide clusters shown in Figures 13a and 13c may relate to earthquakes that are not known from the historical record and thus are worth further investigation. We also note that many landslides were likely induced along the Kashihe Fault by the 1812 Nilke Earthquake, whereas no massive landslides were found near the relocated epicenters of the 1944 Xinyuan Earthquake. We believe several factors can explain this difference. First, the magnitude difference is probably the most significant factor. The 1812 Nilke Earthquake likely had a magnitude of at least Mw 7.5, considerably larger than the 1944 double-event (max. Mw 7.4). Earthquakes of Mw > 7.5 are capable of triggering landslides over a much larger area than those triggered by Mw ∼7 events. Second, the rupture length of the 1812 earthquake may be longer than that of the 1944 double-event, or the epicenter of the 1812 event may be shallower, producing stronger ground shaking. However, we do not have further observations or evidence to confirm these parameters. Third, the terrain near the 1944 epicenters within the Awulale Shan may be inherently less susceptible to large-scale landsliding than the slopes along the Kashihe Fault, due to differences in slope geometry, lithology, and pre-existing failure conditions. These factors may all contribute to the difference in landslide magnitudes between the two earthquakes.

The earthquakes highlight some important features of the seismotectonics of the BRS. The northern margin is dominated by approximately east-west reverse faulting, whereas the southern margins include oblique right-lateral faults with a WNW-ESE trend and left-lateral faults with a WSW-ENE trend (Figures 2 and 16). The interior of the range contains the southern extension of the Dzhungarian right-lateral fault (Campbell et al., 2013; Z. Hu, Yang, et al., 2021). Left-lateral shearing parallel to the Tien Shan range is introduced due to the motion of the Tarim Basin relative to Eurasia (Figures 1a and 16) (Wang & Shen, 2020; Zubovich et al., 2010). The BRS is situated between two separate but major left-lateral fault strands: to the east, the Gobi-Tien Shan Fault system extends into Mongolia, and to the west, left-lateral faulting appears in the high mountainous interior of the Kyrgyz Tien Shan (e.g., the Nalati Fault, Wang et al., 2025, Figure 16). Those two fault zones are offset in strike, which

should lead to transpression across the BRS. The right-lateral Dzhungarian and Kashihe Faults extend southwards into the BRS, and south of the BRS right-lateral faults of the Turfan Basin continue, though again with an offset between the two fault zones that imply transpression across the BRS. Though all of the major faults appear to be truncated to some extent within the BRS itself, and it is unclear as to which are the dominant structures, it seems likely that the topography of the BRS is related to shortening and bookshelf style kinematics within the complex arrangement of left-lateral and right-lateral faulting.

Other right-lateral faults with an NW-SE to NNW-SSE trend are present throughout the Tien Shan and Altay ranges, from the Talas-Fergana Fault of western Tien Shan to the Fuyun and Har-Us-Nuur Faults of western Mongolia (Figure 16: Nissen et al., 2009; Xu et al., 2012; Bande et al., 2017). These right-lateral faults are consistent with a bookshelf kinematic model, where they can both accommodate N-S shortening related to the overall India-Eurasia collision, whilst also enabling distributed range-parallel left-lateral shear in this region (Bayasgalan et al., 2005; Campbell et al., 2015; Cobbold & Davy, 1988; Cunningham, 2005, 2007; Wu et al., 2020, 2021). The regions southeast of the BRS seem to show eastwards block extrusion kinematics, consistent with the overall left-lateral shearing, with the deformation concentrated at the deep crust-cutting strike-slip faults (e.g., Ren et al., 2021) (Figure 16). Since the BRS is an important feature of the India-Eurasia collision zone, involving reverse faulting and both left- and right-lateral strike-slip faulting just like a smaller scale of the Tien Shan, unraveling the tectonic history of the BRS hence has the potential to unravel the tectonic history of the wider Tien Shan and surroundings.

7. Conclusions

We present revised source parameters for three major historical earthquakes, the 1906 Manas, 1944 Xinyuan, and the 1812 Nilke Earthquakes in the BRS, eastern Tien Shan, by integrating published data with remote sensing and seismological analysis. Our study advances the understanding of these events in several key respects. We found that the most common surface deformations associated with these three historical earthquakes are landslides instead of fault scarps, especially for those in the southern BRS. For the 1906 Manas Earthquake, our re-estimated magnitude (Mw 7.7 ± 0.2), relocated epicenter, and identification of coseismic surface ruptures together suggest that this event nucleated on a steeply-dipping basement reverse fault and propagated to the surface across a shallow decollement. For the 1944 Xinyuan Earthquake, our seismological analysis confirms it as a double-event, comprising an Mw 6.5 ± 0.3 foreshock and an Mw 7.2 ± 0.2 main shock at ∼24 km depth, both dominated by strike-slip motion. This revises the previous single-event interpretation and provides new seismological constraints, indicating that both events were dominated by strike-slip motion consistent with several candidate structures in the region. For the 1812 Nilke Earthquake, we propose oblique right-lateral slip on the Kashihe Fault and a splay fault to the south, with a magnitude likely smaller than previously reported. The earthquakes highlight the importance of right-lateral and reverse faulting in the seismotectonics of the BRS, which has formed at an intersection between both left-lateral and right-lateral faults, and which likely accommodate a combination of N-S shortening and range-parallel left-lateral shear by bookshelf faulting and block extrusion. These findings contribute to the broader understanding of how deformation is partitioned within intraplate orogenic belts such as the Tien Shan, where complex fault interactions and seismicity continue to pose significant hazard.

Conflict of Interest

The authors declare no conflicts of interest relevant to this study.

Availability Statement

Scanned seismograms are the property of the University of Potsdam and are accessible via these links (https://seismic-data.geo.uni-potsdam.de/scratch/galina/1906-12-22_ALL.tar.gz and https://seismic-data.geo.uni-potsdam.de/scratch/galina/1944_03_09_ALL.tar.gz).

Acknowledgments
This research was supported by the UK National Environment Research Council (NERC)-funded Centre for the Observation and Modeling of Earthquakes, Volcanoes and Tectonics (COMET) (GA/13/M/031), by NERC-ESRC Increasing Resilience to Natural Hazards programs "Earthquakes without Frontiers" (NE/J02001X/1) and "Seismo-tectonics in Ningxia, Gansu and Shaanxi (STINGS)" (NE/N012313/1), by the NATO Science for Peace and Security Multi-Year program "Environmental security in Kazakhstan and Kyrgyzstan" (G5690), and by the Leverhulme Trust Research Project Grant "EROICA" (RPG-2018-371).

References

Abdrakhmatov, K. E., Aldazhanov, S. A., Hager, B. H., Hamburger, M. W., Herring, T. A., Kalabaev, K. B., et al. (1996). Relatively recent construction of the tien Shan inferred from GPS measurements of present-day crustal deformation rates. *Nature*, *384*(6608), 450–453. https://doi.org/10.1038/384450a0

Abdrakhmatov, K. E., Weldon, R. J., Thompson, S. C., Burbank, D. W., Ch, R., Miller, M., & Molnar, P. (2001). Origin, direction, and rate of modern compression of the central tien Shan (Kyrgyzstan). *Russian Geology and Geophysics*, *42*(10), 1585–1609.

Abe, K. (1981). Magnitudes of large shallow earthquakes from 1904 to 1980. *Physics of the Earth and Planetary Interiors*, *27*(1), 72–92. https://doi.org/10.1016/0031-9201(81)90088-1

Abe, K. (1988). Magnitudes and origin times from milne seismograph data: Earthquakes in China and California, 1898-1912. *Symposium on Historical Seismograms and Earthquakes*, 37–50.

Abe, K., & Noguchi, S. (1983). Revision of magnitudes of large shallow earthquakes, 1897-1912. *Physics of the Earth and Planetary Interiors*, *33*(1), 1–11. https://doi.org/10.1016/0031-9201(83)90002-X

Aki, K. (1966). Generation and propagation of G waves from the Niigata earthquake of June 16, 1964.: Part II. Estimation of earthquake moment, released energy, and stress-strain drop from the G wave spectrum. In *Bulletin of the earthquake research Institute, university of Tokyo* (Vol. 44, pp. 73–88). The Earthquake Research Institute, University of Tokyo. Retrieved from https://ci.nii.ac.jp/naid/120000871042/en/

Avouac, J.-P., Tapponnier, P., Bai, M., You, H., & Wang, G. (1993). Active faulting and folding along the northern tien Shan and late Cenozoic rotation of the tarim relative to Dzungaria and Kazakhstan. *Journal of Geophysical Research*, *98*(B4), 6755–6804. https://doi.org/10.1029/92jb01963

Bai, M., & Fang, Z. (1981). Relationship between phenomena of surface breaking and geological studies of the manas Southwestern earthquake (M=8) in 1906 in the Xinjiang region (in Chinese). *Northwestern Seismological Journal*, *3*(2), 100–102.

Bande, A., Sobel, E. R., Mikolaichuk, A., & Torres Acosta, V. (2017). Talas–fergana fault Cenozoic timing of deformation and its relation to Pamir indentation. *Geological Society, London, Special Publications*, *427*(1), 295–311. https://doi.org/10.1144/SP427.1

Bayasgalan, A., Jackson, J. A., & McKenzie, D. (2005). Lithosphere rheology and active tectonics in Mongolia: Relations between earthquake source parameters, gravity and GPS measurements. *Geophysical Journal International*, *163*(3), 1151–1179. https://doi.org/10.1111/j.1365-246X.2005.02764.x

Berberian, M. (1982). Aftershock tectonics of the 1978 Tabas-e-Golshan (iran) earthquake sequence: A documented active "thin- and thick-skinned tectonic" case. *Geophysical Journal International*, *68*(2), 499–530. https://doi.org/10.1111/j.1365-246X.1982.tb04912.x

Blaser, L., Krüger, F., Ohrnberger, M., & Scherbaum, F. (2010). Scaling relations of earthquake source parameter estimates with special focus on subduction environment. *Bulletin of the Seismological Society of America*, *100*(6), 2914–2926. https://doi.org/10.1785/0120100111

Bondár, I., Engdahl, E. R., Villaseñor, A., Harris, J., & Storchak, D. (2015). ISC-GEM: Global instrumental earthquake catalogue (1900-2009), II. Location and seismicity patterns. *Physics of the Earth and Planetary Interiors*, *239*, 2–13. https://doi.org/10.1016/j.pepi.2014.06.002

Bormann, P., Wendt, S., & DiGiacomo, D. (2013). Seismic sources and source parameters. In *New manual of seismological observatory practice* (Vol. 2, pp. 1–259). German Research Centre for Geosciences (GFZ)

Burchfiel, B. C., Brown, E. T., Deng, Q., Feng, X., Li, J., Molnar, P., et al. (1999). Crustal shortening on the margins of the tien Shan, Xinjiang, China. *International Geology Review*, *41*(8), 665–700. https://doi.org/10.1080/00206819909465164

Cadek, O. (1987). Studying earthquake ground motion in prague from wiechert seismograph records. *Gerlands Beiträge Zur Geophysik*, *96*(5), 438–447.

Campbell, G. E., Walker, R. T., Abdrakhmatov, K. E., Jackson, J. A., Elliott, J. R., Mackenzie, D., et al. (2015). Great earthquakes in low strain rate Continental interiors: An example from SE Kazakhstan. *Journal of Geophysical Research: Solid Earth*, *120*(8), 5507–5534. https://doi.org/10.1002/2015JB011925

Campbell, G. E., Walker, R. T., Abdrakhmatov, K. E., Schwenninger, J., Jackson, J. A., Elliott, J. R., & Copley, A. (2013). The Dzhungarian fault: Late Quaternary tectonics and slip rate of a major right-lateral strike-slip fault in the northern tien Shan region. *Journal of Geophysical Research: Solid Earth*, *118*(10), 5681–5698. https://doi.org/10.1002/jgrb.50367

Charreau, J., Avouac, J.-P., Chen, Y., Dominguez, S., & Gilder, S. (2008). Miocene to present kinematics of fault-bend folding across the huerguosi anticline, northern tianshan (china), derived from structural, seismic, and magnetostratigraphic data. *Geology*, *36*(11), 871–874. https://doi.org/10.1130/G25073A.1

Charreau, J., Saint-Carlier, D., Dominguez, S., Lavé, J., Blard, P. H., Avouac, J.-P., et al. (2017). Denudation outpaced by crustal thickening in the eastern tianshan. *Earth and Planetary Science Letters*, *479*, 179–191. https://doi.org/10.1016/j.epsl.2017.09.025

China Earthquake Administration. (1971). *Catalogue of earthquakes in China (in Chinese)*. Science Press. Retrieved from https://books.google.co.uk/books?id=Cb2CmgEACAAJ

Cobbold, P. R., & Davy, P. (1988). Indentation tectonics in nature and experiment. 2. Central Asia. *Bull. Geol. Inst. Univ. Uppsala, NS*, *14*(June), 143–162.

Cunningham, W. D. (2005). Active intracontinental transpressional Mountain building in the Mongolian Altai: Defining a new class of orogen. *Earth and Planetary Science Letters*, *240*(2), 436–444. https://doi.org/10.1016/j.epsl.2005.09.013

Cunningham, W. D. (2007). Structural and topographic characteristics of restraining Bend Mountain ranges of the Altai. *Gobi Altai and easternmost Tien Shan. Geological Society Special Publication*, *290*(1), 219–237. https://doi.org/10.1144/SP290.7

Daëron, M., Avouac, J.-P., & Charreau, J. (2007). Modeling the shortening history of a fault tip fold using structural and geomorphic records of deformation. *Journal of Geophysical Research*, *112*(3), 1–19. https://doi.org/10.1029/2006JB004460

Daniell, J. E., Schaefer, A. M., & Wenzel, F. (2017). Losses associated with secondary effects in earthquakes. *Frontiers in Built Environment*, *3*, 30. https://doi.org/10.3389/fbuil.2017.00030

De Grave, J., Buslov, M. M., & Van den haute, P. (2007). Distant effects of india–eurasia convergence and Mesozoic intracontinental deformation in central Asia: Constraints from apatite fission-track thermochronology. *Journal of Asian Earth Sciences*, *29*(2), 188–204. https://doi.org/10.1016/j.jseaes.2006.03.001

Deng, Q., Feng, X., Yang, X., Peng, S., Zhang, P., & Xu, X. (1994). Study on Holocene paleoearthquakes by large trench in the manas-tugulu reverse fault and fold zone along northern margin of the tianshan Mountain, in Xinjiang (in Chinese). In *Research on active fault (3)* (pp. 1–16). Seismological Press.

Deng, Q., Feng, X., Yu, H., Chen, J., Li, J., Zhang, Y., et al. (1991). Paleoseismology and late Quaternary activity of the dushanzi-anjihai reverse fault zone, Xinjiang (in Chinese). In *Research on active fault (1)* (pp. 37–56). Science Press.

Deng, Q., Feng, X., Zhang, P., Xu, X., Yang, X., Peng, S., & Li, J. (2000). *Active tectonics of the Chinese tianshan Mountains (in Chinese)*. Seismological Press.

Deng, Q., Zhang, P., Xu, X., Yang, X., Peng, S., & Feng, X. (1996). Paleoseismology of the northern Piedmont of tianshan Mountains, northwestern China. *Journal of Geophysical Research B: Solid Earth*, *101*(3), 5895–5920. https://doi.org/10.1029/95jb02739

Dziewonski, A. M., Chou, T.-A., & Woodhouse, J. H. (1981). Determination of earthquake source parameters from waveform data for studies of global and regional seismicity. *Journal of Geophysical Research*, *86*(B4), 2825–2852. https://doi.org/10.1029/JB086iB04p02825

Ekström, G., Nettles, M., & Dziewonski, A. M. (2012). The global CMT project 2004–2010: Centroid-moment tensors for 13,017 earthquakes. *Physics of the Earth and Planetary Interiors*, *200–201*, 1–9. https://doi.org/10.1016/j.pepi.2012.04.002

England, P., & Molnar, P. (1997). The field of crustal velocity in Asia calculated from Quaternary rates of slip on faults. *Geophysical Journal International*, *130*(3), 551–582. https://doi.org/10.1111/j.1365-246x.1997.tb01853.x

European Space Agency Sinergise. (2021). Copernicus global digital elevation model. Distributed by OpenTopography. https://doi.org/10.5069/G9028PQB

Fang, L., Wu, J., Wang, C., Wang, W., & Yang, T. (2014). Relocation of the 2012 M s6.6 Xinjiang xinyuan earthquake sequence. *Science China Earth Sciences*, *57*(2), 216–220. https://doi.org/10.1007/s11430-013-4755-6

Feng, X. (1987). Paleoseismological study for kaxhe fault zone, Xinjiang. *Seismology and Geology*, *9*(2), 75–77.

Feng, X. (1990). The nilka earthquake fault zone in Xinjiang (in Chinese). *Inland Earthquake*, *4*(3), 5.

Feng, X., Ma, J., Zhou, Y., England, P., Parsons, B., Rizza, M. A., & Walker, R. T. (2020). Geomorphology and paleoseismology of the weinan fault, Shaanxi, central China, and the source of the 1556 huaxian earthquake. *Journal of Geophysical Research: Solid Earth*, *125*(12), e2019JB017848. https://doi.org/10.1029/2019JB017848

Fu, X., Li, S. H., Li, B., & Fu, B. (2017). A fluvial terrace record of late Quaternary folding rate of the anjihai anticline in the northern Piedmont of tian Shan, China. *Geomorphology*, *278*(October), 91–104. https://doi.org/10.1016/j.geomorph.2016.10.034

Gong, W., Zhang, Y., Li, T., Wen, S., Zhao, D., Hou, L., & Shan, X. (2019). Multi-sensor geodetic observations and modeling of the 2017 Mw 6.3 jinghe earthquake. *Remote Sensing*, *11*(18), 2157. https://doi.org/10.3390/rs11182157

Gong, Z., Li, S. H., & Li, B. (2015). Late Quaternary faulting on the manas and hutubi reverse faults in the northern foreland basin of tian Shan, China. *Earth and Planetary Science Letters*, *424*, 212–225. https://doi.org/10.1016/j.epsl.2015.05.030

Grützner, C., Campbell, G. E., Walker, R. T., Jackson, J. A., Mackenzie, D., Abdrakhmatov, K. E., & Mukambayev, A. (2019). Shortening accommodated by thrust and strike-slip faults in the ili basin, northern tien Shan. *Tectonics*, *38*(7), 2255–2274. https://doi.org/10.1029/2018TC005459

Gu, G. (1983). *Catalogue of Chinese earthquakes, 1831 B.C.-1969 A.D. (in Chinese)*. Science Press.

Gutenberg, B., & Richter, C. F. (1942). Earthquake magnitude, intensity, energy and accelaration. *Bulletin of the Seismological Society of America*, *32*(3), 163–190. https://doi.org/10.1086/622062

Gutenberg, B., & Richter, C. F. (1954). *Seismicity of the Earth and associated phenomena, 2nd ed*. Princeton University Press.

Gutenberg, B., & Richter, C. F. (1956). Magnitude and energy of earthquakes: Annali di. *Annali di Geofisica*, *9*(1), 1–15. https://doi.org/10.4401/ag-5590

Hu, G., Chen, J., Zhang, W., Di, N., Li, Y., & Li, S. H. (2021). Out-of-Sequence backthrusting since the middle Pleistocene revealed by the jiangnanmiao thrust fault along the northern tian Shan, China. *Tectonics*, *40*(4), 1–18. https://doi.org/10.1029/2020tc006662

Hu, J., & Bai, M. (1988). The rupture zone of manas earthquake, xingjiang, research on earthquake faults in China (in, edited by *Seismological bureau of xingjiang*. Xingjiang Press, (pp. 61–65).

Hu, Z., Li, T., Thompson Jobe, J., & Yang, X. (2021). Lower portion rupture of a thrust fault during the 2017 Mw 6.3 jinghe earthquake: Implications to seismic hazards in the tian Shan region. *Seismological Research Letters*, *92*(4), 2134–2144. https://doi.org/10.1785/0220200295

Hu, Z., Yang, X., Yang, H., Huang, W., Wu, G., Miao, S., & Zhang, L. (2021). Slip rate and paleoseismology of the Bolokenu-Aqikekuduk (dzhungarian) right-lateral strike-slip fault in the northern tian Shan, NW China. *Tectonics*, *40*(8), e2020TC006604. https://doi.org/10.1029/2020TC006604

Huang, W. L. (2015). *Crustal shortening rates across the yanqi basin, TianShan during mid-late Quaternary (in Chinese)*. Institute of Geology.

Hughes, A. N., & Shaw, J. H. (2014). Fault displacement-distance relationships as indicators of contractional fault-related folding style. *AAPG Bulletin*, *98*(2), 227–251. https://doi.org/10.1306/05311312006

Institute of Geophysics, SSB and Institute of Chinese Historical Geography, F, U. (1990). *Atlas of the historical earthquakes in China (the qing dynasty period) (in Chinese)*. China Cartographic Publishing House.

ISC. (2021). ISC-GEM earthquake catalogue. https://doi.org/10.31905/d808b825

ISC. (2022a). ISC-EHB dataset. https://doi.org/10.31905/PY08W6S3

ISC. (2022b). On-line bulletin. https://doi.org/10.31905/D808B830

Kanamori, H. (1977). The energy release in great earthquakes. *Journal of Geophysical Research (1896-1977)*, *82*(20), 2981–2987. https://doi.org/10.1029/JB082i020p02981

Kárník, V. (1962). Amplitude-distance curves of surface waves at short epicentral distances (Δ<2000 km). *Studia Geophysica et Geodaetica*, *6*(4), 340–346. https://doi.org/10.1007/BF02585233

Kennett, B. L. N., Engdahl, E. R., & Buland, R. (1995). Constraints on seismic velocities in the Earth from traveltimes. *Geophysical Journal International*, *122*(1), 108–124. https://doi.org/10.1111/j.1365-246X.1995.tb03540.x

Kimball, S., Mattis, P., Natterer, M., & Neumann, S. (2013). GIMP: G image manipulation program. Version 2.8. Retrieved from http://www.gimp.org/

Klinger, Y., Etchebes, M., Tapponnier, P., & Narteau, C. (2011). Characteristic slip for five great earthquakes along the fuyun fault in China. *Nature Geoscience*, *4*(6), 389–392. https://doi.org/10.1038/ngeo1158

Kulikova, G. (2016). *Source parameters of the major historical earthquakes in the tien-shan region from the late 19th to the early 20th century*. University of Potsdam.

Kulikova, G., & Krüger, F. (2015). Source process of the 1911 M8.0 chon-kemin earthquake: Investigation results by analogue seismic records. *Geophysical Journal International*, *201*(3), 1891–1911. https://doi.org/10.1093/gji/ggv091

Lee, J.-C., & Chan, Y.-C. (2007). Structure of the 1999 chi-chi earthquake rupture and interaction of thrust faults in the active fold belt of Western Taiwan. *Journal of Asian Earth Sciences*, *31*(3), 226–239. https://doi.org/10.1016/j.jseaes.2006.07.024

Li, C. X., Guo, Z., & Dupont-Nivet, G. (2011). Late Cenozoic tectonic deformation across the northern foreland of the Chinese tian Shan. *Journal of Asian Earth Sciences*, *42*(5), 1066–1073. https://doi.org/10.1016/j.jseaes.2010.08.009

Li, J., Feng, X., Chen, J., Zhao, R., Deng, Q., Tang, W., et al. (1992). Activity of the huoerguos active fold and thrust fault zone (in Chinese). In *Research on active fault (2)* (pp. 105–116).

Li, Y., Si, S., Lu, S., & Wang, Y. (2012). Tectonic and climatic controls on the development of the kuitun river terraces in the northern Piedmont of tianshan Mountains (in Chinese). *Quaternary Sciences*, *32*(5), 880–890.

Liu, C.-J. (1961). A graticule for the macroseismic determination of the depth of focus of an earthquake. *Chinese Journal of Geophysics*, *10*(2), 114–119.

Long, W., Li, Z., Wang, Y., Almeida, R., Camanni, G., Sun, C., et al. (2025). Role of active folding in rupture arrest of a great thrust earthquake. *Geophysical Research Letters*, *52*(18), e2025GL117527. https://doi.org/10.1029/2025GL117527

Lu, R., He, D., Xu, X., Wang, X., Tan, X., & Wu, X. (2018). Seismotectonics of the 2016 M 6.2 hutubi earthquake: Implications for the 1906 M 7.7 Manas Earthquake in the northern tian Shan belt, China. *Seismological Research Letters*, *89*(1), 13–21. https://doi.org/10.1785/0220170123

Mackenzie, D., Elliott, J. R., Altunel, E., Walker, R. T., Kurban, Y. C., Schwenninger, J., & Parsons, B. (2016). Seismotectonics and rupture process of the MW 7.1 2011 Van reverse-faulting earthquake, eastern Turkey, and implications for hazard in regions of distributed shortening. *Geophysical Journal International*, *206*(1), 501–524. https://doi.org/10.1093/gji/ggw158

Middleton, T., Walker, R. T., Parsons, B., Lei, Q., Zhou, Y., & Ren, Z. (2015). A major, intraplate, normal-faulting earthquake: The 1739 yinchuan event in northern China. *Journal of Geophysical Research: Solid Earth*, *4*(1), 293–320. https://doi.org/10.1002/2015JB012355

Molnar, P., & Deng, Q. (1984). Faulting associated with large earthquakes and the average rate of deformation in central and eastern Asia. *Journal of Geophysical Research*, *89*(B7), 6203–6227. https://doi.org/10.1029/jb089ib07p06203

Molnar, P., & Tapponnier, P. (1975). Cenozoic tectonics of Asia: Effects of a Continental collision. *Science*, *189*(4201), 419–426. https://doi.org/10.1126/science.189.4201.419

Mooney, W. D., Laske, G., & Masters, T. G. (1998). Crust 5.1: A global crustal model at 5° x 5°. *Journal of Geophysical Research*, *103*(B1), 727–747. https://doi.org/10.1029/97jb02122

Nissen, E., Walker, R. T., Bayasgalan, A., Carter, A., Fattahi, M., Molor, E., et al. (2009). The late Quaternary slip-rate of the har-us-nuur fault (mongolian Altai) from cosmogenic 10Be and luminescence dating. *Earth and Planetary Science Letters*, *286*(3–4), 467–478. https://doi.org/10.1016/j.epsl.2009.06.048

Nowicki Jessee, M. A., Hamburger, M. W., Ferrara, M. R., McLean, A., & FitzGerald, C. (2020). A global dataset and model of earthquake-induced landslide fatalities. *Landslides*, *17*(6), 1363–1376. https://doi.org/10.1007/s10346-020-01356-z

Ou, Q., Kulikova, G., Yu, J., Elliott, A. J., Parsons, B., & Walker, R. T. (2020). Magnitude of the 1920 haiyuan earthquake reestimated using seismological and geomorphological methods. *Journal of Geophysical Research: Solid Earth*, *125*(8), e2019JB019244. https://doi.org/10.1029/2019JB019244

Pang, L., Lu, H., Wu, D., Guan, X., Zhao, J., Zheng, X., & Li, Y. (2021). Late Pleistocene uniform rate of thrusting along the fault's strike: A case study from the northern tian Shan foreland. *Tectonics*, *40*(4), 1–23. https://doi.org/10.1029/2021tc006726

Ren, G., Li, C., Wu, C., Zhang, H., Wang, S., Ren, Z., et al. (2021). Late Quaternary slip rate and kinematics of the baoertu fault, constrained by 10Be exposure ages of displaced surfaces within eastern tian Shan. *Lithosphere*, *2021*(1), 1–19. https://doi.org/10.2113/2021/7866920

Richter, C. F. (1958). *Elementary seismology*. W. H. Freeman.

Schweitzer, J. (2001). HYPOSAT – An enhanced routine to locate seismic events. *Pure and Applied Geophysics*, *158*(1), 277–289. https://doi.org/10.1007/PL00001160

Schweitzer, J. (2012). User manual for HYPOSAT and HYPOMOD. *New Manual of Seismological Observatory Practice*, *2*, 1–38.

Seismological Bureau of Xinjiang. (1985). *Compilation of seismic data in Xinjiang uygur autonomous region (in Chinese)* (pp. 38–44). Seismological Press.

Shen, J., Wang, Y., Li, Y., Jiang, H., & Xiang, Z. (2003). Late Quaternary right-lateral strike-slip faulting along the Bolokenu-Aqikekuduke fault in Chinese tian Shan. *Seismology and Geology*, *25*(2), 183–194.

Sloan, R. A., Jackson, J. A., McKenzie, D., & Priestley, K. (2011). Earthquake depth distributions in central Asia, and their relations with lithosphere thickness, shortening and extension. *Geophysical Journal International*, *185*(1), 1–29. https://doi.org/10.1111/j.1365-246X.2010.04882.x

Stockmeyer, J. M., Shaw, J. H., Brown, N. D., Rhodes, E. J., Richardson, P. W., Wang, M., et al. (2017). Active thrust sheet deformation over multiple rupture cycles: A quantitative basis for relating terrace folds to fault slip rates. *Bulletin of the Geological Society of America*, *129*(9–10), 1337–1356. https://doi.org/10.1130/B31590.1

Stockmeyer, J. M., Shaw, J. H., & Guan, S. (2014). Seismic hazards of multisegment thrust-fault ruptures: Insights from the 1906 Mw 7.4-8.2 manas, China, earthquake. *Seismological Research Letters*, *85*(4), 801–808. https://doi.org/10.1785/0220140026

Storchak, D., Di Giacomo, D., Bondár, I., Engdahl, E. R., Harris, J., Lee, W. H. K., et al. (2013). Public release of the ISC–GEM global instrumental earthquake catalogue (1900–2009). *Seismological Research Letters*, *84*(5), 810–815. https://doi.org/10.1785/0220130034

Su, P., He, H., Wei, Z., Lu, R., Shi, F., Sun, H., et al. (2018). A new shortening rate across the dushanzi anticline in the northern tian Shan Mountains, China from LiDAR data and a seismic reflection profile. *Journal of Asian Earth Sciences*, *163*(June), 131–141. https://doi.org/10.1016/j.jseaes.2018.06.008

Walker, R., Jackson, J., & Baker, C. (2003). Surface expression of thrust faulting in eastern Iran: Source parameters and surface deformation of the 1978 tabas and 1968 ferdows earthquake sequences. *Geophysical Journal International*, *152*(3), 749–765. https://doi.org/10.1046/j.1365-246X.2003.01886.x

Wang, C. Y., Yang, Z. E., Luo, H., & Mooney, W. D. (2004). Crustal structure of the northern margin of the eastern tien Shan, China, and its tectonic implications for the 1906 M~7.7 manas earthquake. *Earth and Planetary Science Letters*, *223*(1–2), 187–202. https://doi.org/10.1016/j.epsl.2004.04.015

Wang, L., Ren, Z., He, Z., Ji, H., Liu, J., Guo, L., & Li, X. (2025). Strong earthquakes of the strike-slip nalati fault within the tianshan orogenic belt. *Tectonics*, *44*(12), e2025TC008960. https://doi.org/10.1029/2025TC008960

Wang, M., & Shen, Z. K. (2020). Present-day crustal deformation of Continental China derived from GPS and its tectonic implications. *Journal of Geophysical Research: Solid Earth*, *125*(2), e2019JB018774. https://doi.org/10.1029/2019JB018774

Wang, Q., Ji, Z., Zhao, C., Wang, H., Nie, X., & Li, Z. (2015). Research on source rupture process of Ms 6.6 earthquake of June 30, 2012, in the border area of xinyuan and hejing county, Xinjiang (in Chinese). *Seismology and Geology*, *37*(1), 33–43.

Wang, X., Xu, C., Wen, Y., Wang, S., Xu, G., Xiao, Z., & Fang, L. (2019). The 2016 Mw 6.0 hutubi earthquake: A blind thrust event along the northern tian Shan front. *Journal of Asian Earth Sciences*, *173*(December 2018), 79–87. https://doi.org/10.1016/j.jseaes.2019.01.011

Wells, D. L., & Coppersmith, K. J. (1994). New empirical relationships among magnitude, rupture length, rupture width, rupture area, and surface displacement. *Bulletin of the Seismological Society of America*, *84*(4), 974–1002. https://doi.org/10.1785/bssa0840040974

Wesnousky, S. G. (2008). Displacement and geometrical characteristics of earthquake surface ruptures: Issues and implications for seismic-hazard analysis and the process of earthquake rupture. *Bulletin of the Seismological Society of America*, *98*(4), 1609–1632. https://doi.org/10.1785/0120070111

Windley, B. F., Alexeiev, D., Xiao, W., Kroner, A., & Badarch, G. (2007). Tectonic models for accretion of the Central Asian orogenic belt. *Journal of the Geological Society*, *164*(1), 31–47. https://doi.org/10.1144/0016-76492006-022

Windley, B. F., Allen, M. B., Zhang, C., Zhao, Z.-Y., & Wang, G.-R. (1990). Paleozoic accretion and Cenozoic redeformation of the Chinese tien Shan range, central Asia. *Geology*, *18*(2), 128–131. https://doi.org/10.1130/0091-7613(1990)018<0128:PAACRO>2.3.CO;2

Wu, C., Ren, G., Yu, J., Zheng, W., Li, X., Liu, J., et al. (2020). Oblique right-lateral faulting along the northern margin of the ili basin in the northern tian Shan, northwest China. *Tectonics*, *39*(10), 1–22. https://doi.org/10.1029/2020TC006061

Wu, C., Wang, W., Zheng, W., Zhang, P., & Yu, Z. (2021). Opposite sense of strike-slip faulting and crustal rotation accommodating left-lateral shear between the tianshan Mountains and Kazakh platform. *Geophysical Research Letters*, *48*(24), 1–8. https://doi.org/10.1029/2021GL096442

Xie, Y. S., & Cai, M. B. (1986). *Collections of historical records of earthquakes in China (in Chinese)*. Science Press.

Xu, X., Sun, X. Z., Tan, X., Li, K., Yu, G., Etchebes, M., et al. (2012). Fuyun fault: Long-term faulting behavior under low crustal strain rate (in Chinese). *Seismology and Geology*, *34*(4), 606–617. https://doi.org/10.3969/j.issn.0253-4967.2012.04.007

Yang, X., Deng, Q., Zhang, P., Xu, X., Yu, G., & Feng, X. (1998). Active reverse fault-fold zones and estimation of potential earthquake sources in northern tianshan (in Chinese). *Seismology and Geology*, *20*(3), 194–200.

Yang, X., Gu, M., Sun, Z., Zhao, C., & Zhou, Q. (2002). Multilayered reverse faults and deep structures in the manas earthquake area, northern TianShan (in Chinese). *Seismology and Geology*, *24*(3), 304–314.

Yang, Z. (1988). The preliminary study of the landslides triggered by historial earthquakes in Xinjiang (in Chinese). *Journal of Seismology*, *3*, 1–8.

Yang, Z. (1992). Discussion on the epicentral position of xinyuan earthquake with magnitude 7.25 on march 10. 1944. *Earthquake Research in China*, *8*(2), 29–37. (in Chinese).

Yang, Z., Cheng, X., Yin, G., Li, J., & Zhang, Y. (1985). The nilke great earthquake (M=8.0), march 8, 1812, Xinjiang) (in Chinese). *Northwestern Seismological Journal*, *7*(1), 60–65.

Yin, G., Jiang, J. X., & Pei, H. D. (2006). The fault and the maximal displacement of nilike earthquake in 1812 (in Chinese). *Inland Earthquake*, *20*(4).

Yin, G., Jiang, J. X., & Wu, G. (2009). Research of the Macro-epicenter location on 1812 nilka earthquake (in Chinese). *Inland Earthquake*, *23*(4), 425–429.

Yin, G., Jiang, J. X., Zhang, Y., & Li, J. (2002). The character of seismic fault of 1812 nileke earthquake (in Chinese). *Northwestern Seismological Journal*, *24*(2), 4. https://doi.org/10.18907/jjsre.4.Special_87_1

Yin, G., Li, J., Zhang, Y., & Yang, Z. (2001). Statistical analysis and research of landslides caused by nileke earthquake (in Chinese). *Inland Earthquake*, *15*(1), 57–63.

Zelenin, E., Bachmanov, D., Garipova, S., Trifonov, V., & Kozhurin, A. (2021). The database of the active faults of eurasia (AFEAD): Ontology and design behind the continental-scale dataset. https://doi.org/10.5194/essd-2021-312

Zhang, P., Deng, Q., Xu, X., Peng, S., Yang, X., Feng, X., et al. (1994). Blind thrust, folding earthquake, and the 1906 manas earthquake, Xinjiang (in Chinese). *Seismology and Geology*, *16*(3), 193–204.

Zhang, P., Deng, Q., Xu, X., Wu, Z., Li, J., Chen, W., et al. (1994). Tectonic deformation, crustal shortening, and slip rate estimation along the manas reverse fault-fold zone (in Chinese). In *Research on active fault (3)* (pp. 18–31). Seismological Press.

Zhou, W., Yang, Z. E., Sun, J., & Zhao, R. (2003). Numerical modeling of the generation process of the 1906 manas Ms 7.7 earthquake (in Chinese). *Seismology and Geology*, *25*(4), 610–616.

Zubovich, A. V., Wang, X. Q., Scherba, Y. G., Schelochkov, G. G., Reilinger, R. E., Reigber, C., et al. (2010). GPS velocity field for the tien Shan and surrounding regions. *Tectonics*, *29*(6), 1–23. https://doi.org/10.1029/2010TC002772